General Geometry Computed Tomography Reconstruction

by

Alexei Ramotar

A thesis
presented to the University of Waterloo
in fulfilment of the
thesis requirement for the degree of
Master of Mathematics
in
Computer Science

Waterloo, Ontario, Canada, 2006

I hereby declare that I am the sole author of this thesis. This is a true copy of the thesis, including any required final revisions, as accepted by my examiners.

I understand that my thesis may be made electronically available to the public.

Abstract

The discovery of Carbon Nanotubes and their ability to produce X-rays can usher in a new era in Computed Tomography (CT) technology. These devices will be lightweight, flexible and portable. The proposed device, currently under development, is envisioned as a flexible sheet of tiny X-ray emitters and detectors. The device is wrapped around an appendage to acquire X-ray projections and reconstruct a CT image. However, current CT reconstruction algorithms can only be used if the geometry of the CT device is regular (usually circular). We present an efficient and accurate reconstruction technique that is unconstrained by the geometry of the CT device. Indeed the geometry can be both regular and highly irregular. To evaluate the feasibility of reconstructing a CT image from such a device, a simulation test bed was built to generate simulated CT ray sums of an image. This data was then used in our reconstruction method. The reconstruction method consists of resampling the irregular X-ray projection onto a regular grid, whereupon the Filtered Backprojection method can be used. Our method depends on the ability to know the locations of the X-ray emitters and detectors; we foresee integrating a shape-tracking device into the CT-scanner. In anticipation that a real-world implementation of such a device will have to be robust to measurement errors, we have conducted tests to analyze how our reconstructions behave in the presence of errors. Observations of reconstructions, as well as quantitative results, suggest that this simple method is efficient and accurate.

Acknowledgments

I would like to thank Dr. Jeff Orchard of the Scientific Computing group at the University of Waterloo for his guidance and encouragement without which this thesis would not have been possible. I would also like to express thanks to Canadian Commonwealth Scholarship and Fellowship Awards Program for funding my studies as a Masters student at the University of Waterloo.

I am also grateful for the support of friends who I met during my studies at the University specifically, Maja Omanovic, Omar Halabieh, Dalia Krieger, Sami Khachan, David Brown and Bassam Aoun whose friendship and advice allowed for a memorable and entertaining stay in Canada.

Dedication

For my family.

Contents

List of Tables

List of Figures

Chapter 1

Introduction

With the discovery of Carbon Nanotubes (CNT) in 1991 by the Japanese physicist Sumio Iijima [1], followed by the discovery of Nanotubes as field emitters in 1995 [2] scientists at the University of North Carolina were able to produce X-rays in 2001 [3]. Researchers have therefore been able to miniaturize X-ray emitters. In this thesis we envision a device where X-ray emitters and detectors are attached to some flexible fabric that can be placed around an appendage or a body and a Computed Tomography (CT) scan obtained. Current reconstruction algorithms are based on the device having a circular geometry. However, the envisioned device will create geometries that are highly irregular.

This thesis, while anticipating a CNT technology that can effectively create X-ray beams powerful enough to penetrate layers of tissue, is focused on developing a reconstruction algorithm that does not rely on the geometry of the scanner.

1.1 Carbon Nanotubes

Like diamond, and graphite, CNT's are a pure molecular configuration of carbon atoms, known as *carbon allotropes*. Carbon Nanotube molecules are cylindrical and, together with their synthesis process, result in unique properties. These include

impressive strength and high electric and thermal conductivity. There are two types of nanotubes; Single Walled Nanotubes (SWNT) and Multi-walled Nanotubes (MWNT). Single Walled Nanotubes are formed by taking a single sheet of graphite, one atom thick, and rolling it up, like a sheet of paper, to form a cylinder. Multi-walled Nanotubes are formed by rolling up several sheets. Because of the fact that SWNTs are used to create X-rays, we will focus on SWNTs. Further reading including synthesis can be found in [4, 5, 6, 7].

In the following sections we give short descriptions of the major properties of CNTs (see [4, 5, 6, 7] for more detail).

1.1.1 Strength of CNT

Carbon Nanotubules are incredibly strong primarily due to their structure and the fact that the carbon bonds in graphite are some of the strongest chemical bonds known. As a matter of fact, CNTs are currently the strongest known fibers. This strength is manifest both interms, tensile strength (the force required to pull it apart to breaking point), and modulus of elasticity (the force necessary to cause deformation). However, its structure also contributes to its weakness under compression. Because the molecule is hollow, under a compressive force it will buckle.

1.1.2 Electric Conductivity

The electric property of a CNT depends on its structure. All armchair structures (Fig 1.1) result in metallic fibers, while others like chiral have both semiconductor and metallic characteristics. In metallic CNTs the conductivity can be better than copper. Superconductivity has also been observed in CNTs [9]. This is due to the crystalline structure of the CNT, where electrons flow through the material without collisions, called *Ballistic conduction*. Bending and twisting of CNTs produces various electric properties.
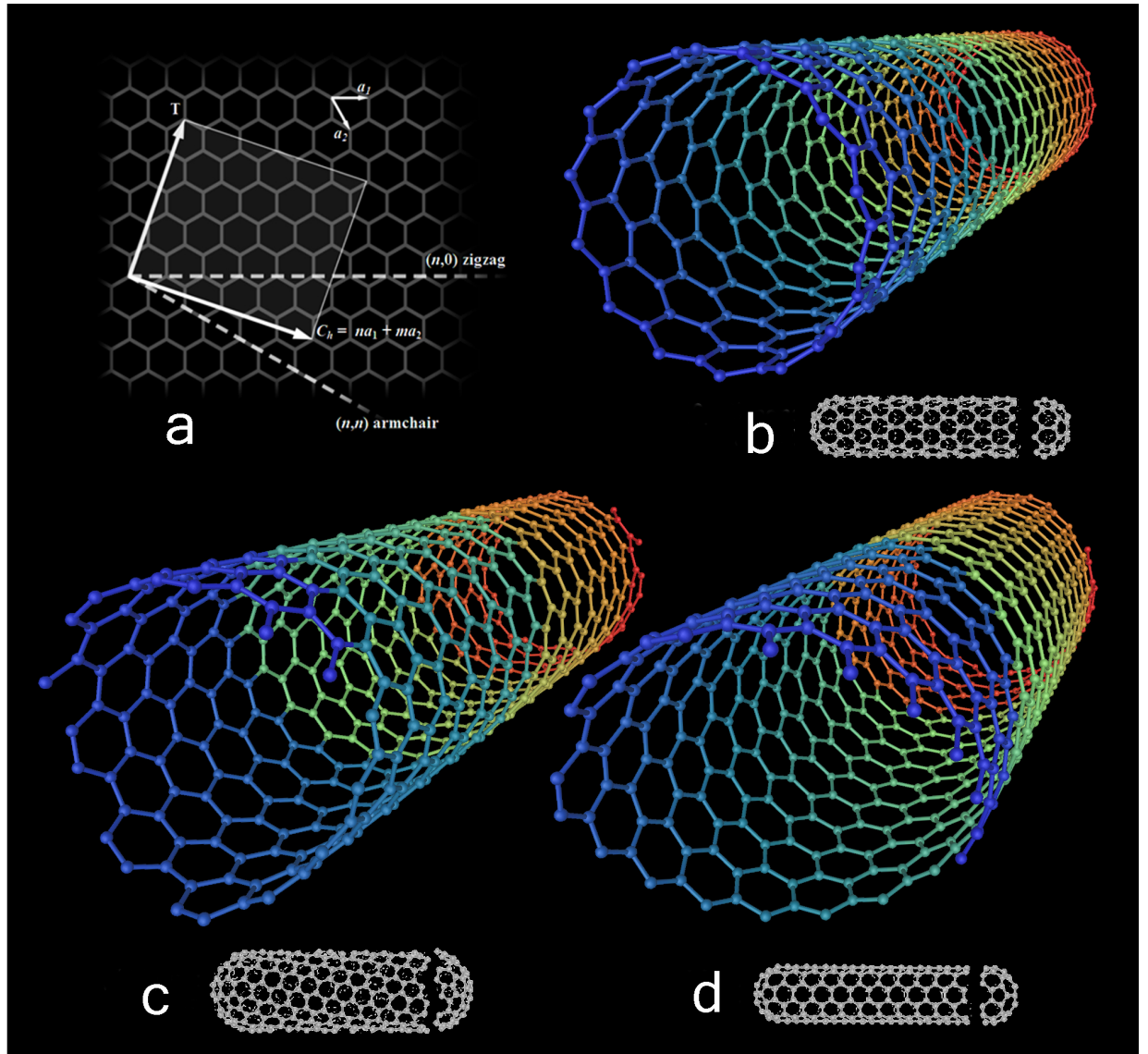
Figure 1.1: The different ways a graphite sheet can be rolled up. The integers a_1 and a_2 in a) represent unit vectors, n and m are integers and T is the tube axis. b) shows a zig-zag configuration c) a chiral and d) an armchair configuration. These configuration results in the wide difference in observed properties. For example, all armchair configurations result in a metallic nanotube while others result in a semiconductors [8].

1.1.3 Thermal Conductivity

As in the case of Electric Conductivity, thermal conductivity depends on the configuration and ballistic conduction. Like graphite and diamond, CNTs have high thermal conductivity. However, the structure also affects conductivity with chiral configured molecules having higher conductivity [10, 11].

1.2 Carbon Nanotubues in Diagnostic Imaging

In traditional X-ray generation the cathode is heated causing the electrons on the surface to break free of their bonds, a process known as *thermionic emission* [12, 13]. An electric potential is then applied that causes these electrons to accelerate, hit a piece of metal, usually tungsten, and release X-rays. This process is described in the following chapter. Unfortunately this process requires a lot of energy and the intense heat, in excess of $2000°C$, quickly degrades the cathode tube. However, a quantum process called *field emission* releases electrons from a surface, in the presence of a high electric field, at room temperature. Field emission is dependent on the type of material and shape, such that materials with a high aspect ratio create a larger current. Carbon Nanotubes are perfect candidates for field emission as they can be very good conductors and their tops are capped. With synthesis this cap can be made more pointy and thereby generate a higher current. The current obtained from field emission follows the Fowler-Nordheim relation

$$I(V) = \frac{1.56 \times A \times 10^{-6} \times V^2}{\varpi} \exp\left(-\frac{6.83 \times 10^7 \times \varpi^{1.5}}{V}\right), \qquad (1.1)$$

where V is the applied voltage, A emitting surface area, and ϖ the work function.

In 2002 researchers at the University of North Carolina were able to use CNTs to generate X-rays and obtain the images of a fish and a hand shown in Fig 1.2 [3].
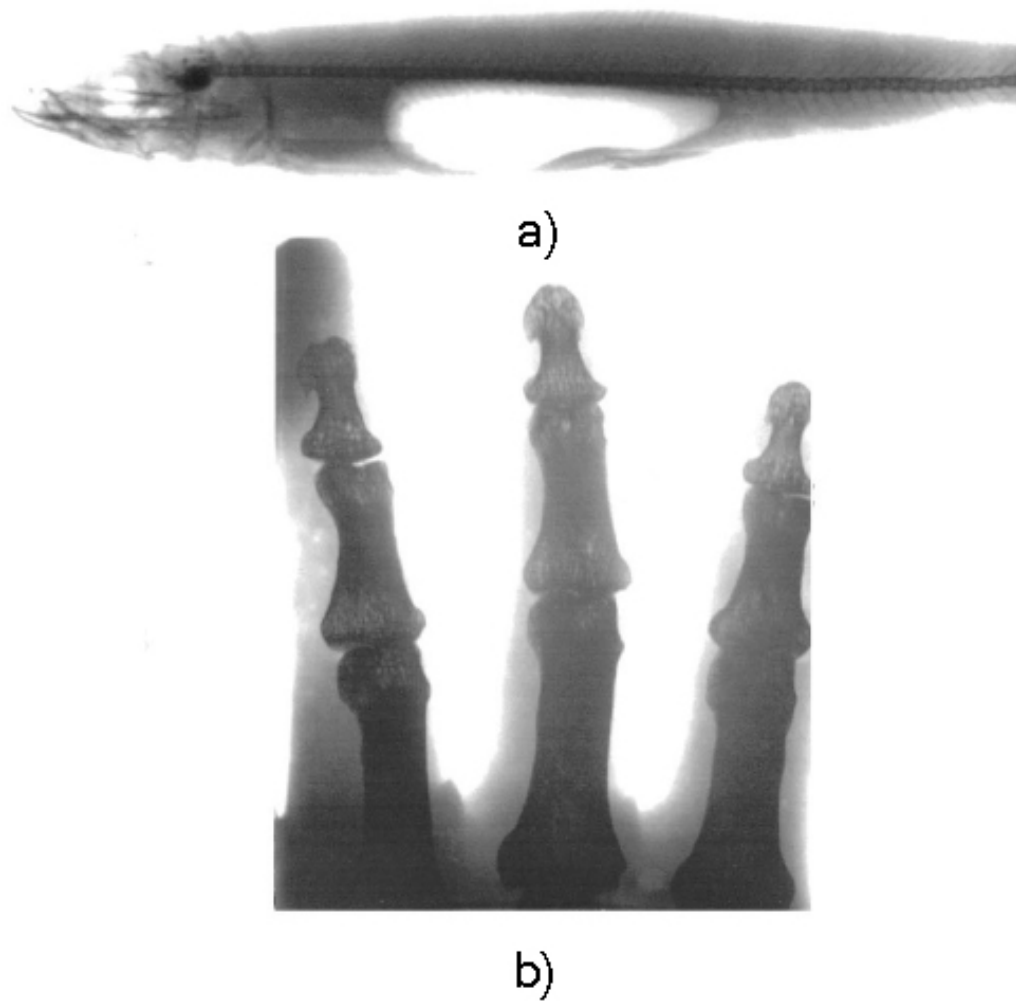
Figure 1.2: X-ray images obtained from a CNT device using 14kV at a distance of 30cm from the objects. a) a fish, b) fingers [3].

1.3 Current CT technology

The first commercially available CT-scanner was developed by Godfrey Hounsfield in 1972. The first clinical scanner was installed in 1974 and only performed head scans. However, by 1976 full body scanners were available. Hounsfield's first scanner used arithemetic reconstruction techniques to reconstruct the image. This technique took hours to reconstruct a single slice and days to obtain volumes. Below we provide a quick overview of the evolution of CT scanners.

1.3.1 First Generation

These CT scanners used a thin beam of radiation directed at one or two detectors. A slice of an object was acquired by a method where the X-ray source and the detector are in a fixed relative position and move across the patient followed by a rotation of the gantry by one degree, and another set of translations. In Houndsfield's original scanner, called the EMI-Scanner, a pair of images was acquired in about 4 minutes with the gantry rotating a total of 180 degrees.

1.3.2 Second Generation

In this design the number of emitters and detectors on the gantry was increased. This allowed the use of a fan beam to cover larger areas and decrease imaging time. Rotation of the gantry was increased from 1 to 30 degrees. Otherwise the mechanism remained similar to first generation machines.

1.3.3 Third Generation

Third generation increased the coverage of the fan beam. Also the detectors were fixed, thus allowing for scanning of a larger area and eliminating the need for the gantry to translate and rotate. Now it only needed to rotate. This dramatically decreased scanning time and for the first time allowed the imaging of the lungs and other vacilatting organs (Fig. 1.3).

1.3.4 Fourth Generation

Fourth Generation scanners have detectors 360° around the gantry and only the emitter moves. Although imaging time did not improve, the ring artifact problem was solved. The ring artifact is due to faulty calibration of a detector resulting in erroneous reading at each angular position. This results in a circular artifact in the reconstructed image.
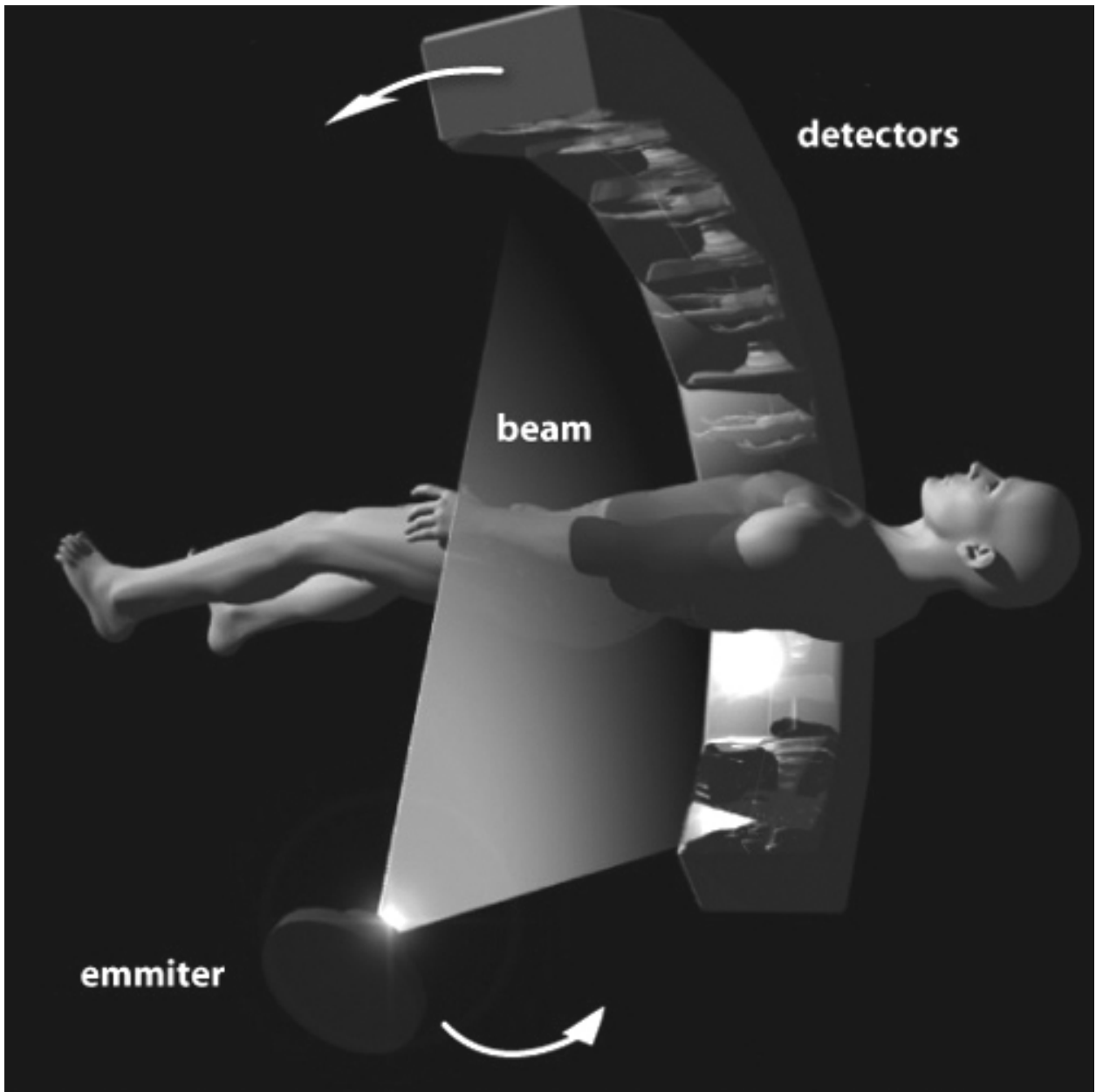
Figure 1.3: Third generation scanner. A group of detecors and an emitter source are mounted on a gantry. Using fanbeam projection, the data is collected. The gantry is then rotated by a certain amount and another projection taken. Going through a 180° or 360° circle gives one slice of the abdomen. The smaller the degree of rotation the better quality the image, however it takes a longer time to obtain [14].

Chapter 2

Theory of CT Reconstruction

2.1 Physics of X-rays

In this chapter we go through some of the very basics of X-ray physics with the primary aim in deriving the equation

$$I = I_0 e^{\mu} L. \tag{2.1}$$

This equation is the fundamental equation in CT mathematics that is used to derive the Radon Transform [15]. The Radon Transform (in particular its inverse) is the means by which image reconstruction is obtained.

X-rays are electromagnetic radiation similar to microwaves, visible light, ultraviolet light and radio waves. However, X-rays (along with γ rays) are the only form of electromagnetic radiatation that have the potential of liberating electrons from their atomic bonds [16]. The wavelength of X-rays ranges from a few picometers (10^{-9} meters) to nanometers (10^{-6} meters) [16]. The energy contained in an X-ray photon is given by [17]

$$E = hv = \frac{hc}{\lambda}, \tag{2.2}$$

where h is Planck's constant ($\approx 6.63 \times 10^{-34}$Js) [17], and c is the speed of light ($\approx$ 2.997925$x10^8$m/s). This equation shows that the energy of an X-ray is inversely proportional to its wavelength λ. That is, the longer the wavelength the lower the energy of the X-ray photons. In a CT scan, the operation of the X-ray tube, and the energy of the ejected photons, is measured in units kilo-Volts potential (kVp). Therefore a tube operating at 1Vp produces an X-ray photon of 1eV (1.602×10^{-19}J) accelerated across an electrical potential of 1V. Diagnostic X-rays operate in the range of 12.4kVp to 140kVp corresponding to X-rays of wavelengths between 0.1nm to 0.01nm [16, 18]. Longer wavelength X-rays, called soft X-rays, do not have the necessary energy to penetrate deep into materials, while shorter wavelengths too easily penetrate materials resulting in very little contrast between materials and are therefore not used.

X-ray photons can be produced several different ways; however, most radiology departments use the X-ray tube. The X-rays are produced when a substance, usually tungsten, is bombarded by high speed electrons resulting in different types of interactions occuring. The two major types of X-rays produced by an X-ray tube are the Bremsstrahlung radiation and Characteristic X-rays. It is worthy to note that 99% of the input energy in an X-ray tube is converted to heat. This is because the majority of the encounters are the transfer of energy from the incident electron to the target atom's electron. These types of encounters give rise to only heat and no X-ray photons.

2.1.1 Bremsstrahlung Radiation

Bremsstrahlung radiation, shown in Fig. 2.1, is produced when the incident electrons intereact with the nuclei of an atom. This interaction occurs in one of two ways as shown in the diagram. When an incident electron passes close to the nucleus of an atom the difference in charges causes the electron to decelerate. This rapid deceleration of the electron gives rise to the Bremsstrahlung radiation. The intensity of this radiation is also dependent on how close to the nucleus, specifically how deep within the coulomb field, the electron passes. The further away, the
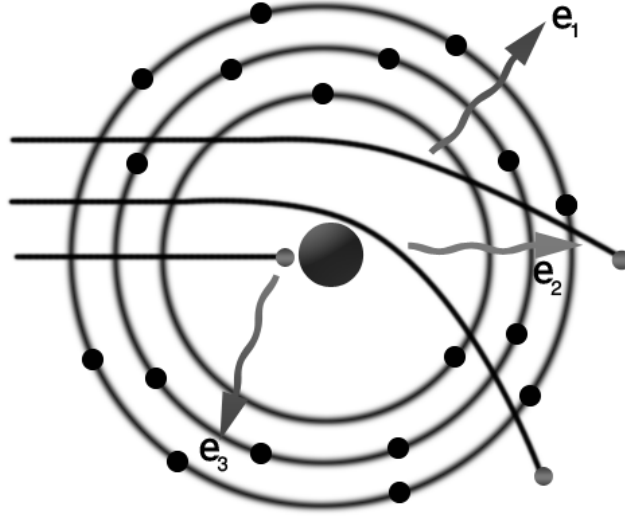
Figure 2.1: Bremsstrahlung Radiation

lower the energy of Bremsstrahlung radiation [19, 20]. The total intensity of the Bremsstrahlung radiation is proportional to Ze, the charge of the target nuclei that comes into contact with an incident particle of charge ze and mass m. Here Z is the atomic number of the target nuclei, z is the atomic number of the incident particle and e is the *elementary charge* which is a constant of value $\approx 1.602 \times 10^{-19}$C [17]. Note that for an electron this value is negative.

$$I \propto \frac{Z^2 z^4 e^6}{m^2}. \tag{2.3}$$

Equation 2.3 [16] indicates why electrons, and not protons or alpha particles, are used to create the radiation. The mass of an electron makes it 3 million times more efficient. Equation 2.3 also indicates that Bremsstrahlung production increases as the atomic number of the target increases.

Bremsstrahlung radiation is also produced when an incident electron hits the nuclei of a target atom. In this interaction, the entire energy of the incident electron is transferred into bremsstrahlung radiation. This interaction represents the upper part of the energy spectrum as shown in Fig. 2.2. However, as shown in Fig. 2.2,

11
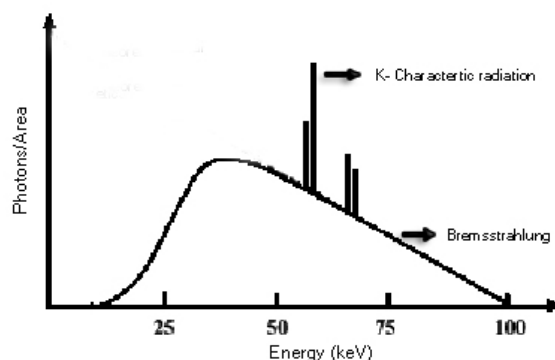
Figure 2.2: X-ray spectra produced by 100keV electrons incident on tungsten. Characteristic X-rays appear as spikes while the remainder is Bremsstrahlung radiation.

there are not many incidents of this nature.

2.1.2 Characteristic X-rays

In Fig. 2.3 we show the classical Bohr model of an atom, where electrons occupy an orbit around the nuclei. Each orbiting electron is in a specific 'shell', with the innermost shell called the K shell. As we proceed to each shell away from the nucleus we increment alphabetically thus having L, M, N and so on. Each electron in the shell has a binding energy. In tungsten for example, the binding energy of the K, L, M, and N shells are 70 keV, 11 keV, 3 keV, and 0.5keV, respectively. See [16] for more details on the structure of an atom.

When atoms are bombarded with incident electrons, some incident electrons will collide with the electrons orbiting the atoms. If, for example, an incident electron is able to knock out an electron from an inner shell, like the K shell, two things occur. First an X-ray photon called the *characteristic radiation* is produced, and secondly an electron from the next outer shell, in this case an L shell, falls into the hole created. This in turn creates another X-ray photon and a domino like effect
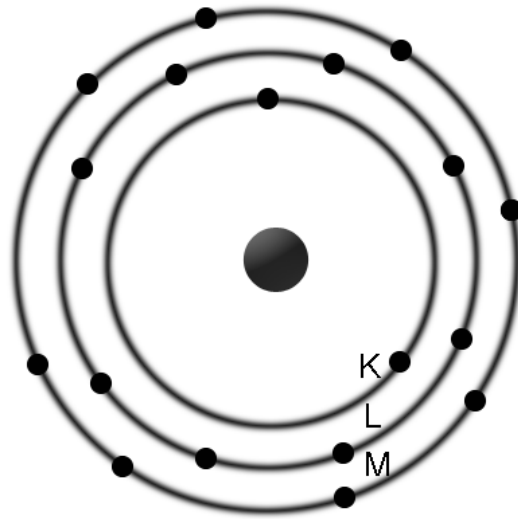
Figure 2.3: The Bohr model of an atom, with a proton-neutron nucleus surrounded by electrons.

occurs. The energy of this characteristic X-ray is equal to the difference between the binding energies of the K and L, L and M and so on. Therefore in the case that an electron from the K shell of a tungsten atom is ejected by an incident electron, the energy of the X-ray photon produced is equal to 70 keV - 11 keV = 59keV. It should be noted that each element in the periodic table has its own unique shell binding energies and thus the energies of the X-ray photons are unique for each atom, hence the name characteristic X-rays. It should also be noted that the low level X-rays produced by the domino effect are absorbed within the X-ray tube. This process is called X-ray filtration (see [16, 21] for details).

So far we have looked at the two types of X-rays produced in a cathode tube. In the following sections we will look at the interactions that occur within atoms as a result of incident X-rays.
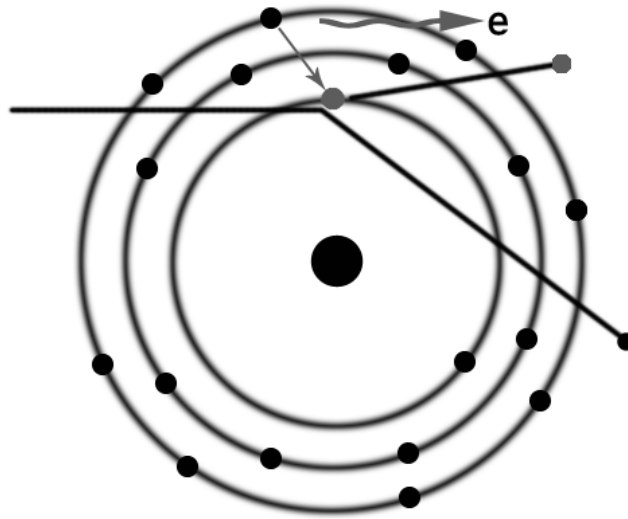
Figure 2.4: A graphical view of the photoelectric effect.

2.1.3   X-Ray Interactions

Medical CT machines use X-rays that typically have photon energies between 12.4keV and 140keV. In this range there are three ways in which X-rays interact with matter: 1) The Photoelectric Effect, 2) Rayleigh scattering and 3) Compton effect.

The *photoelectric effect* first described by Albert Einstein in 1905 states that an electron can be ejected from its orbit around an atom if the incident electromagnetic radiation is equal to or greater than the binding energy of the atomic shell of that specific electron, the X-ray photon energy is absorbed by the electron [22, 23, 24]. In our case the incident electromagnetic radiation is the X-ray photon. As explained in the above section the loss of an electron will cause a domino effect creating characteristic X-rays. However, unlike an X-ray tube where tungsten is used, the constituent parts of the human body have relatively small atomic numbers. While tungsten's atomic number is 74, that of calcium (the major constituent in bone) is only 20. Thus the characteristic X-rays produced by the photoelectric effect have very low energies (that of bone is 4keV) resulting in quick absorption within the

14

body. Typically an X-ray of 1eV is absorbed by about 2.7μm of tissue. Figure. 2.4 shows this process.

The photoelectric effect, however, plays an important role in obtaining contrast between different tissues. The probability of photoelectric interaction is proportional to the cube of the atomic number Z,

$$P_{\text{photoelectric}} \propto Z^3. \tag{2.4}$$

Therefore tissues with small differences in atomic numbers result in greater differences in the probability of the photoelectric effect occuring, resulting in different absorption of X-ray photons.

The second type of interaction is called the *Rayleigh scattering* [16]. It occurs when the incident photon does not have enough energy to cause the photoelectric effect and there is no transfer of energy. Rayleigh scattering does, however, alter the trajectory of the photon, thus broadening the swath of the X-ray beam. This suggests that higher energy X-rays should produce a lot less scattering than lower energies, which is indeed the case (see [16, 23]). Although traditionally Rayleigh scattering has only been considered a nuisance in CT imaging, research at Robarts Research Institute (London, Ontario) is trying to use the effects of scattering to create material-specific maps of tissues such as bones [25, 26].

The third type of interaction, *Compton scattering* [16], involves the collision of an X-ray photon with an electron from the outer shell of the atom. In this type of collision the photon retains most of its energy while some is transferred to the electron, thus freeing it from its bond. Figure 2.5 shows Compton scattering. The incident X-ray photon is scattered over an angle $\theta \in [0°, 180°]$. Low energy incident photons are usually being back scattered (scatter $> 90°$). Unlike the photoelectric effect, the probability of Compton scattering depends on the electron density in the material, and since many body tissues tend to have similar electron densities, this type of interaction offers little contrast information. Therefore Compton scattering is also regarded as a nuisance and medical CT devices try to minimize its impact in various ways [16, 26].
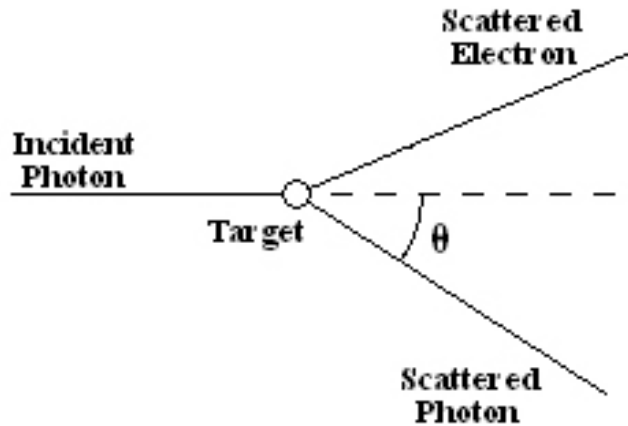
Figure 2.5: A graphical view of Compton scattering.

A fourth kind of interaction called *Pair and Triplet production* also occurs. However, it is only feasible at levels above 1.02MeV, well above the energies used in CT devices [16].

2.1.4 Attenuation

The interaction mechanisms mentioned above all combine to change the strength of the X-rays as they pass through the body. The photoelectric effect dominates the lower energy levels up to 50 keV, while the Compton effect dominates above 90 keV; between these extremes they are both important. These effects cause *attenutation*, the removal of X-ray photons from a beam by absorbtion or scattering. To show the effects of attenuation let us imagine a piece of uniform material with thickness dx. For a given chemical environment there is a probability associated with each interaction, called the attenuation coefficient. Let κ, σ and σ_r be the attenuation coefficients of the photoelectric, Compton and Rayleigh scattering in the material. The sum of these interactions is

$$\mu = \kappa + \sigma + \sigma_r. \tag{2.5}$$

16

Thus μ is the probability that an incident photon will be attenuated (removed) from the beam while traversing one unit of thickness of the material. Let I be a beam of X-ray photons incident on our material. Then as the beam penetrates the material the change in its intensity, dI, can be written as

$$dI = -\mu I dx. \tag{2.6}$$

Letting $dx \to 0$, and integrating this differential equation leads to

$$\int_{I_0}^{I} dI/I = -\mu \int_{0}^{x} dx, \tag{2.7}$$

which gives us the Beer-Lambert law

$$I = I_0 e^{-\mu x}, \tag{2.8}$$

where I_0 is the intensity of the incident beam. Thus we have the intensity of the X-ray exiting a material is a function of the material thickness and the attenuation coefficients[1]. From this equation we see that the higher the μ value, the smaller I and therefore higher the attenuation. However, the body is not composed of uniform material so we will consider the case for nonuniform materials. We can take this nonuniform material and divide it into thin slices of thickness Δx, and assume that each slice is uniform. Applying the Beer-Lambert law gives

$$I = I_0 e^{-\mu_1 \Delta x} e^{-\mu_2 \Delta x} ... e^{-\mu_n \Delta x} = I_0 e^{\sum_{n=1}^{N} \mu_n \Delta x}, \tag{2.9}$$

which in turn gives us

$$-\ln\left(\frac{I}{I_0}\right) = \sum_{n=1}^{N} \mu_n \Delta x \implies \int_{L} \mu(x) dx \tag{2.10}$$

as Δx approaches 0. This equation states that taking the logarithm of the ratio of the output intensity over the input is equal to the line integral of the attenuation coefficients in the path. This brings us to the Radon Transform. In mathematics

---

[1]This is assuming that the input X-ray photons are monoenergetic.
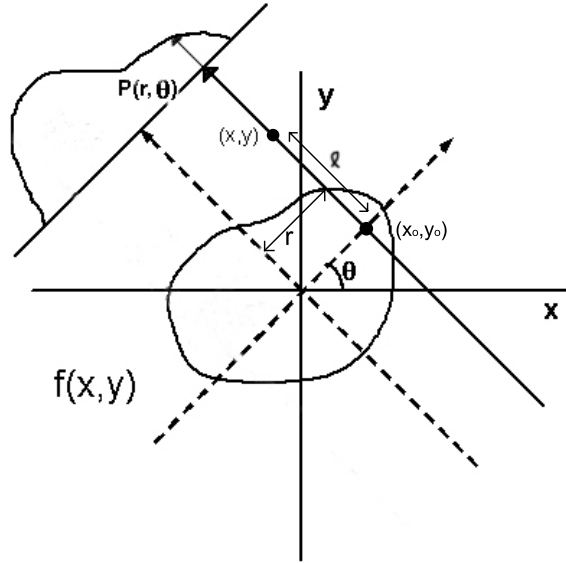
Figure 2.6: The parameters r and t used to specify the position of the beam (line).

the Radon Transform in two dimensions is the integral of a function over a set of lines. As it relates to our work the a line can be viewed as an X-ray beam path.

2.2 CT geometry

Before we begin discussion on the Radon Transform it is good to understand the geometry in which X-rays in a CT machine operate.

In Fig. 2.6, (x, y) are arbitrary points on the photon beam(the line). Using polar coordinates we see that

$$x_0 = r\cos\theta \ , \ y_0 = r\sin\theta. \tag{2.11}$$

The length ℓ is given by

$$\ell = \frac{x - x_0}{\sin\theta} \ , \ \ell = \frac{y - y_0}{\cos\theta}. \tag{2.12}$$

Using (2.11) and (2.12) we get,

$$x = r\cos\theta + \ell\sin\theta, \ y = r\sin\theta + \ell\cos\theta. \tag{2.13}$$

18

These are simultaneous equations and we can therefore easily change (2.13) to obtain

$$r = x\cos\theta + y\sin\theta = (x,y) \cdot (\cos\theta, \sin\theta), \tag{2.14}$$

and

$$\ell = -x\sin\theta + y\cos\theta = (x,y) \cdot (-\sin\theta, \cos\theta). \tag{2.15}$$

2.3 Radon Transform

The Radon Transform is a mathematical analog to the X-ray projection obtained from a CT-scnaeer. In this section we will define the Radon Transform, and show its relationship to the Fourier Transform [27, 15]. We will, however, go into more detail on this relationship in the next section. In Fig. 2.6 the line represents an incident ray passing through an object. The Radon Transform in computed tommography can be simply defined as the collection of line integrals (X-ray beam projections) of the attenuation coefficients of an object. In the 2D case, we represent each line integral as $p(r,\theta)$,

$$p(r,\theta) = \int_{-\infty}^{\infty} f(x,y)d\ell, \tag{2.16}$$

$$\text{where } r = (x,y) \cdot (\cos\theta, \sin\theta), \tag{2.17}$$

and the attenuation coefficient of the object at the point (x,y) is denoted by $f(x,y)$.

To simplify the problem, we use the Dirac δ function, also called the impulse function,

$$\delta(y - y_0) = \begin{cases} 0 & \text{if } y \neq y_0 \\ \text{undefined} & \text{for } y = y_0. \end{cases}$$

The Dirac δ function has an important property; for any function $f(y)$ that is continuous at $y = y_0$,

$$\int_a^b f(y)\delta(y - y_0)dy = \begin{cases} f(y_0) & \text{if } a < y_0 < b \\ 0 & \text{otherwise.} \end{cases}$$

19
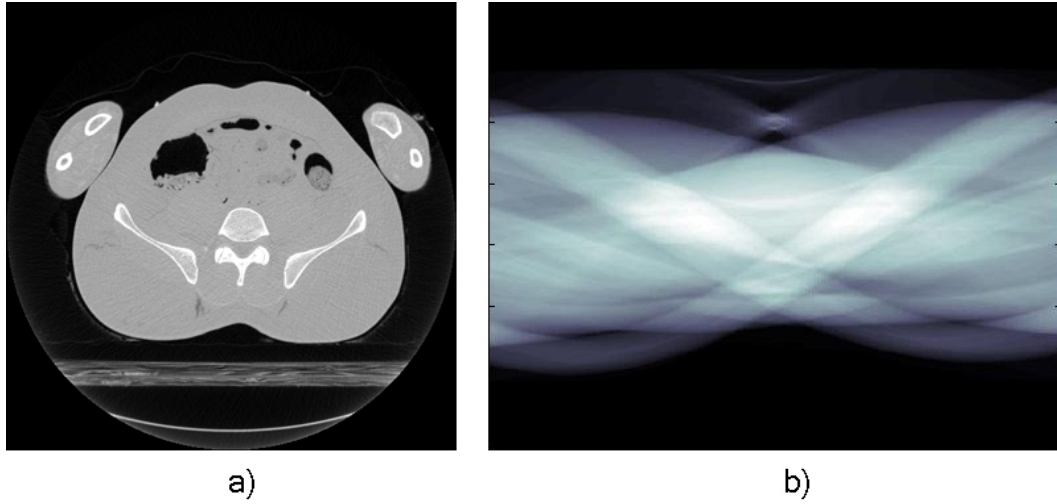
Figure 2.7: A slice of the pelvis and its associated Radon Transform

The equation of the line given by (2.14) and (2.15), together with the above property of the Dirac δ function, gives us

$$p(r, \theta) = \iint_{-\infty}^{\infty} f(x, y)\delta(r - (x, y) \cdot (\cos\theta, \sin\theta))dxdy. \qquad (2.18)$$

Equation (2.18) gives the Radon Transform. As the the source beams are rotated about the object a collection of these integrals will result as seen in Fig. 2.7.

In Chapter 3 we simulate a CT scanner using a ray tracing method to compute the Radon Transform [28].

2.4 Fourier Transform

The Fourier Transform is used to convert an image from the *Spatial domain* to its *Frequency domain*. The spatial domain of an image is the image space where a change in position on the image represents a change in position of the object being

imaged. The frequency domain represents the decomposition of a signal into its frequency components. Each Fourier coefficient in the frequency domain specifies the amplitude and phase of the corresponding wave. For example, let 20 be the value represented at a frequency of 0.1. This means that in the image the intensity values vary from dark to light to dark over a period of 10 pixels (the reciprocal of the frequency), and the contrast between darkest and lightest is 2×20 grey levels. Mathematically the one-dimensional Fourier Transform of $f(x)$ is given by

$$F(u) = \int_{-\infty}^{\infty} f(x)e^{-i2\pi ux}dx, \qquad (2.19)$$

where u is the frequency, and $i = \sqrt{-1}$. To obtain an image from the frequency domain, the inverse Fourier Transform is used,

$$f(x) = \int_{-\infty}^{\infty} F(u)e^{i2\pi ux}du. \qquad (2.20)$$

If, however, the original image $(f(x, y))$ is two-dimensional then we can extend the Fourier Transform to two dimensions. Mathematically this is given by,

$$F(u, v) = \iint_{-\infty}^{\infty} f(x, y)e^{-i2\pi(ux+vy)}dxdy, \qquad (2.21)$$

while the inverse is given by

$$f(x, y) = \iint_{-\infty}^{\infty} F(u, v)e^{i2\pi(ux+vy)}dudv, \qquad (2.22)$$

where u and v are the horizontal and vertical frequencies.

Discrete versions of the Fourier Transform exist, and can be used on sampled data such as images. The two-dimensional discrete Fourier Transform (DFT) is

$$F(u, v) = \frac{1}{N^2} \sum_{x=0}^{N-1} \sum_{y=0}^{N-1} f(x, y)e^{\frac{-2\pi i(ux+vy)}{N}} \; , \; u, v \in [0, N-1], \qquad (2.23)$$

and its inverse is

$$f(x, y) = \frac{1}{N^2} \sum_{x=0}^{N-1} \sum_{y=0}^{N-1} F(u, v)e^{\frac{2\pi i(ux+vy)}{N}} \; , \; x, y \in [0, N-1]. \qquad (2.24)$$

21
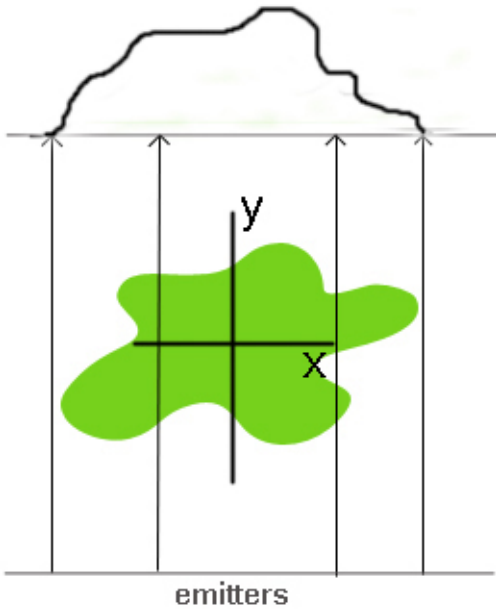
Figure 2.8: Parallel Beam projection at angle $\theta = 0$

2.5 Fourier Slice Theorem

The Fourier Slice Theorem (also called the Central Slice Theorem) [15] in its simplest form states that the one-dimensional Fourier Transform of a Radon projection at an angle θ is equal to a slice through the two-dimensional Fourier Transform of the object. Let $p(x, 0)$ be the Radon Transform of a slice of an object $f(x, y)$ taken at an angle $\theta = 0$. Figure. 2.8 shows a parallel beam projection taken at $\theta = 0$. The Radon Transform is therefore given by,

$$p(x, 0) = \int_{-\infty}^{\infty} f(x, y) dy. \tag{2.25}$$

The one-dimensional Fourier Transform with respect to x of the Radon projection is:

$$\int_{-\infty}^{\infty} p(x,0)e^{-i2\pi ux}dx = \iint_{-\infty}^{\infty} f(x,y)e^{-i2\pi ux}dydx. \qquad (2.26)$$

The two-dimensional Fourier Transform of the slice $f(x,y)$ evaluated at $v = 0$ can be given as

$$\iint_{-\infty}^{\infty} f(x,y)e^{-i2\pi(ux+vy)}dydx\Big|_{v=0} = \iint_{-\infty}^{\infty} f(x,y)e^{-i2ux\pi}dydx. \qquad (2.27)$$

The right hand side of equations (2.26) and (2.27) are identical. Thus we have the Fourier Transform of the projection, taken at an angle $\theta = 0$, equal to the two-dimensional Fourier Transform of a slice, at $v = 0$. Because the coordinate system is arbitrarily selected the above is valid for any rotated coordinate system [27]. Therefore, reconstruction of an image essentially amounts to an inverse of the two-dimensional Fourier Transform. The one-dimension Fourier Transform of all the projections are assembled together in the frequency domain, each projection taking its position as a line through the origin. All These projections together constitute the two-dimensional Fourier Transform of the desired image. hence, an inverse tow-dimensional Fourier Transform reconstructs the image.

2.6   Arithmetic Reconstruction Techniques

Despite the above reletionship between the Fourier Transform and CT reconstruction, the first methods used to reconstruct image slices from CT data used Arithemetic Reconstruction Techniques (ART) [16]. These techniques have now been replaced by the Fourier method described in the previous section. However, it still holds interest for us because it provides a simple explanation of CT reconstruction, as well as for its historical reference. In Fig. 2.9 we show a simple slice of an object divided into 4 pixels: A, B, C, and D represent the unknown attenuation coefficients.

There are two main methods of solving this problem, the first by solving the simultaneous equations as shown in Fig. 2.10 and the second by the iterative reconstruction technique.
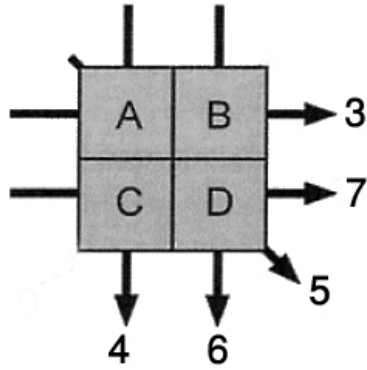
Figure 2.9: A 2x2 pixel slice of an object with unknown attenuation coefficients A,B,C, and D.

$$A + B = 3$$
$$A + C = 4$$
$$A + D = 5$$
$$B + D = 6$$
$$C + D = 7$$

Figure 2.10: Simultaneous equations can be obtained and solved.

Simultaneous equations

As shown in Fig. 2.10 we are able to obtain five simultaneous equations for four unknowns. Elementary algebra tells us that if we have an equal number of unknowns and linear independent equations for the unknowns then it is quite easy to find the values of the unknowns. Therefore for an $N \times N$ pixel image we will need N^2 measurements and therefore that number of equations. The very first CT-machine, in 1967, employed direct matrix inversion to solve 28,000 simultaneous equations. As the need for better spatial resolution increased, there was a corresponding increase in the number of pixels and therefore the number of equations to be solved. Even by today's computing standards this would require an enormous amount of computer power. Furthermore to ensure enough independent equations are formed we often have to take more than N^2 equations. In Fig. 2.9 we see that $B + D = 8$ is not linearly independent:

$$B + D = (A + B) + (C + D) - (A + C). \tag{2.28}$$

In the event that we collect more measurements than we have variables, we can still obtain a solution using optimization methods such as least squares.

Iterative Reconstruction Technique

There are iterative methods for approximating the solution of the linear systemes outlined in the previous section. Here, we give an example. In Fig. 2.11 we have a simple pictorial explanation of iterative reconstruction. Again we will consider a 2×2 slice of an object. Taking the horizontal measurements first (we could alternatively have taken the vertical measurements) we first evenly distribute the sum of the projections ($3 + 7 = 10 \Rightarrow 10/4 = 2.5$). Each pixel is given that average. We then calculate the horizontal line integrals of our initial estimate giving 5, we then compare these line integral values to those obtained from the original object projections. We see that our estimates result in the values of 5 (instead of 3) and again 5 (instead of 7). We observe that the top row is off by 2 and the bottom is
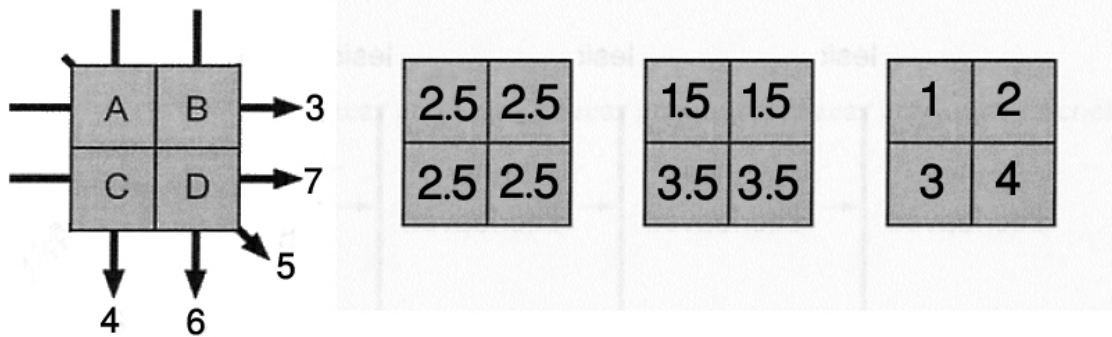
Figure 2.11: Simple example of iterative reconstruction. The average of the sum of all horizontal projections $(7 + 3 = 10)$ is first equally distributed about each pixel. Then the average along a row is compared to the projection data, in the case of the top row we have, difference $= (2.5 + 2.5) - 3 = 2$, and for the bottom row it is $(2.5 + 2.5) - 7 = -2$. The value $\frac{\text{difference}}{\text{no. of pixels in row}}$ is then subtracted from each pixel in its particular row. We do the same thing for all the rows and then for each column. The matrix will have to be modified each time we go through the iterative process resultin in a $O(N^2)$ updates being performed.

off by -2. The difference for each row is split evenly among the pixels in that row: $\frac{\text{difference}}{\text{number of pixels in row}} = 1$, giving 1, and -1 respectively. This process is repeated for projections in the vertical direction. For further reading see [29].

Like the previous method, the calculations of $2N$ equations and N^2 updates is still computationally intensive. Together with the fact that modern CT scanners can acquire a complete projection data set in fractions of seconds and hundreds of images are required for examination, usage of ART is not feasible. However, the fact that they exist provided the pioneers with the knowlege that it is a practically solvable problem.

26

2.7 Filtered Backprojection

The Filtered Backprojection algorithm is used to reconstruct an image from projections [27]. The Fourier Slice Theorem provides a mathematically straighforward solution to the reconstruction method. From the theorem we see that the Fourier Transformation of a projection is a straight line going through the origin in two-dimensional frequency space. This results in samples from the projection falling on a polar coordinate grid. To perform the two-dimension Inverse Fast Fourier Transform the samples will have to be interpolated to a Cartesian coordinate system. However, the data in the frequency domain is typically non-smooth, therefore re-sampling can introduce substantial inaccuracies. A gridding method to perform this process is presented in [30], however the reconstructions produced by this method is not of the quality as that produced by Filtered Backprojection [30].

To get around the issue of interpolating in the frequency domain, we again look at the Fourier Slice Theorem and find an alternative implementation. This alternative is called Filtered Backprojection. The mathematics behind this theorem is described below.

Mathematical Formulation

We will first write down some of the equations given in previous sections.

$$r = x \cos \theta + y \sin \theta \tag{2.29}$$

$$\ell = -x \sin \theta + y \cos \theta. \tag{2.30}$$

Using equation (2.29) we can express the projection in terms of the rotated coordinate system r and ℓ

$$p(r, \theta) = \int_{-\infty}^{\infty} f_\theta(r, \ell) d\ell, \tag{2.31}$$

for each θ. Therfore by the Fourier Slice Theorem we first obtain the one-dimensional Fourier Transform of equation (2.31),

$$P(\omega, \theta) = \iint_{-\infty}^{\infty} f_\theta(r, \ell) d\ell e^{-i2\pi\omega r} dr, \tag{2.32}$$

where ω (the spatial frequency) is measured in radians, for each θ. Using (2.29), (2.32) can be written as

$$P(\omega, \theta) = \iint_{-\infty}^{\infty} f(x, y) e^{-i2\pi\omega(x\cos\theta + y\sin\theta)} dxdy. \tag{2.33}$$

So far we have just found the Fourier Transform of the projections. As the Fourier Slice Theorem states, we now have to find the two-dimensional Inverse Fourier Transformation. In general the two-dimensional Inverse Fourier Transform is given by

$$f(x, y) = \iint_{-\infty}^{\infty} F(u, v) e^{i2\pi(ux+vy)} dudv. \tag{2.34}$$

So we have

$$f(x, y) = \iint_{-\infty}^{\infty} P(\omega, \theta) e^{i2\pi(ux+vy)} dudv. \tag{2.35}$$

The values u and v represents the spacial frequencies of x and y respectively in the frequency domain. We can express u and v in polar coordinates as

$$u = \omega\cos\theta, \ v = \omega\sin\theta. \tag{2.36}$$

Now we do a change of variable from uv to the polar coordinates $\omega\theta$ giving us

$$dudv = \begin{vmatrix} \frac{\delta u}{\delta \omega} & \frac{\delta u}{\delta \theta} \\ \frac{\delta v}{\delta \omega} & \frac{\delta v}{\delta \theta} \end{vmatrix} d\omega d\theta = \omega d\omega d\theta. \tag{2.37}$$

The Jacobian is evaluated to ω. Substituting (2.37) and (2.36) into (2.35) we get

$$f(x, y) = \int_0^{2\pi} \int_0^{\infty} \omega P(\omega, \theta) e^{i2\pi\omega(x\cos\theta + y\sin\theta)} d\omega d\theta. \tag{2.38}$$

We now use (2.29) and obtain

$$f(x, y) = \int_0^{2\pi} \int_0^{\infty} P(\omega, \theta) e^{i2\pi\omega r} \omega d\omega d\theta. \tag{2.39}$$

As stated in an earlier section, the sampling geometry is symmetric giving $p(r, \theta + \pi) = p(-r, \theta)$. The properties of the Fourier Transformation result in

28

this symmetry being transferred to the frequency domain such that $P(\omega, \theta + \pi) = P(-\omega, \theta)$. Applying this symmetry to equation (2.39) results in

$$f(x, y) = \int_0^\pi \int_{-\infty}^\infty P(\omega, \theta) e^{i2\pi\omega r} \mid \omega \mid d\omega d\theta. \tag{2.40}$$

This is the mathematics for the reconstruction of an image given a one-dimensional Fourier Transform of its projection, $P(\omega, \theta)$. In the following section we will explain how Filtered Backprojection is implimented.

Filtered Backprojection Implementation

As the name suggests there are two parts to implementing this algorithm: first we filter the the projection and then backproject the result. The filter is given by the inner integral of equation (2.40),

$$g(r, \theta) = \int_{-\infty}^\infty P(\omega, \theta) e^{i2\pi\omega r} \mid \omega \mid d\omega. \tag{2.41}$$

A popular filter in use is the Ramachandran and Lakshminarayanan (Ram-Lak) filter [27]. This filter emphasizes noise but other filters such as the Hamming, Hanning and Shepp-Logan ([27]), reduce this effect. The Ram-Lak filter is shown in Fig. 2.12.

The ideal filter can not be practically implemented since the gain on this filter is infinite at an infinite frequency. However, ω_{max} is the highest spatial frequency in the projection and therefore we can truncate the function at ω_{max} resulting in the Ram-Lak filter as shown in Fig. 2.12. Therefore the integral, can be written as

$$g(r, \theta) = \int_{-\omega_{\text{max}}}^{\omega_{\text{max}}} P(\omega, \theta) e^{i2\pi\omega r} \mid \omega \mid d\omega. \tag{2.42}$$

The Ram-Lak function is defined as

$$H(\omega) = \begin{cases} \mid \omega \mid & \text{if } -\omega_{max} < \omega < \omega_{max} \\ 0 & \text{otherwise.} \end{cases} \tag{2.43}$$
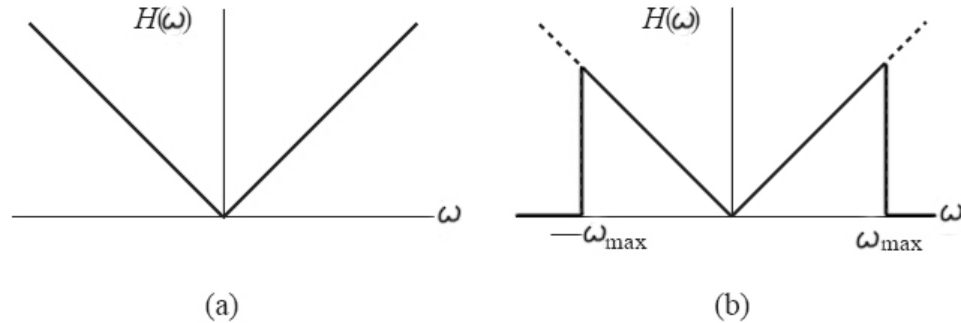
29

Figure 2.12: Filter functions a) Ideal Filter($|\omega|$), b) Ram-Lak Filter

The implementation of the filtering process works by first taking the one-dimensional Fourier Transform of each projection at θ and multiplying each strip by the filter function. The inverse Fourier Transform is then taken of the result. We then apply the backprojection.

Backprojection is depicted in Fig. 2.13. We orient the projection at θ. Then for each pixel we 'draw' a perpendicular line to the point on this projection. The value found on the projection is then added to the pixel, using linear interpolation as needed. Other interpolation methods such as nearest neighbour or splines can also be used.

Backprojection is the process of smearing a projection back over the image. In a sense, it is the opposite of projection, where a two-dimensional image is projected onto a one-dimensional function. Instead, a one-dimensional function is "spread" (like a knife spreads butter) over the image, leaving its one-dimensonal distribution as it goes. Figure 2.14 shows a "spread" at $\theta = 0$.

It should be noted that this method assumes that the projections are generated from a parallel-beam X-ray device. The assumption is implicit in the Radon Transform and its inverse.
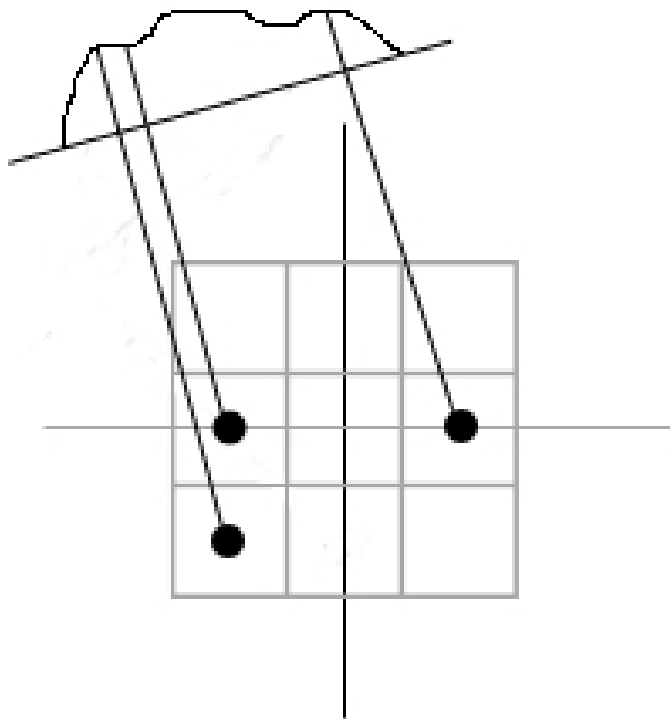
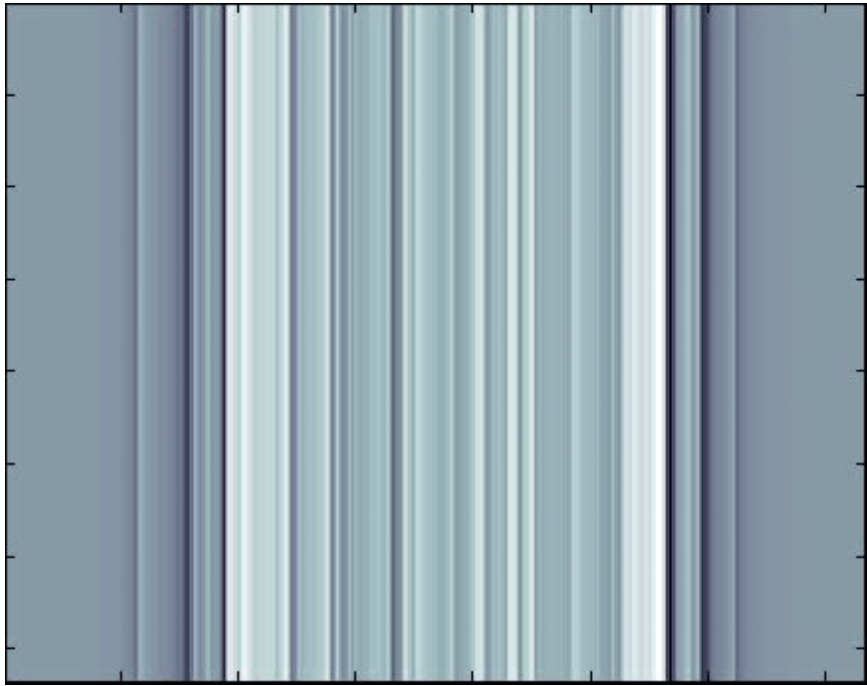Figure 2.13: Backprojection, the value is copied on to all pixels perpendicular to r

Figure 2.14: Backprojection at an angle $\theta = 0$

Chapter 3

Methods and Experiments

In this chapter we propose an algorithm that is used to obtain the reconstruction of an image without consideration for the geometry of the scanner. Our algorithm works if the scanner has rectangular, circular or even incoherent geometry. In a later section we explain in more detail how our data is obtained. This chapter focuses on the algorithm itself.

Our research into various methods of CT-reconstruction brought us to the conclusion that the Filtered Backprojection algorithm, which is well established and studied, should be incorporated. This will help in the implementation process and provides mathematical rigor to our algorithm. Fanbeam projections [27], which are the closest geometry to what our simulation generates, also use a resampling method to obtain data needed to apply the parallel beam based Filtered Backprojection algorithm. However, before applying the Filtered Backprojection algorithm the input data has to be normalized such that implementing the Filtered Backprojection would be seamless.

3.1 General Geometry CT Reconstruction

Figure 3.1 shows the data obtained from our simulation and the same data obtained using standard parallel beam projection. As shown in Fig. 3.1(a) the data obtained
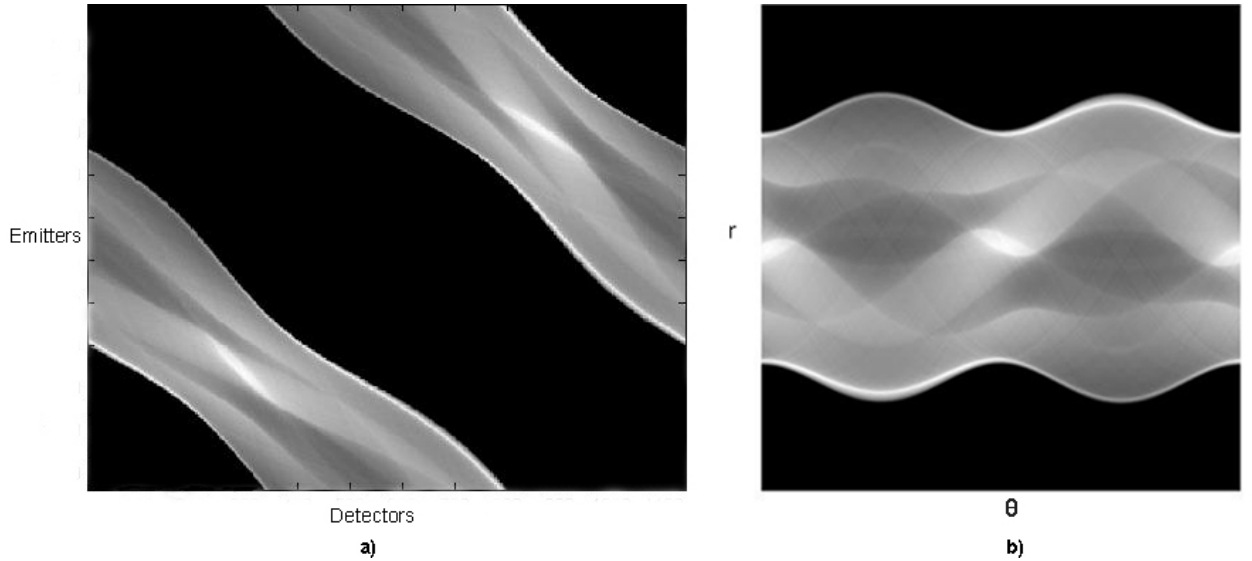
Figure 3.1: Projection data obtained from the Shepp-Logan phantom a) Sample data obtained from our simulation, b) Same data as reconstructed using Matlab's parallel beam simulation.

from our simulation has emitters and detectors as its horizontal and vertical axes respectively. However, the parallel beam data is represented by r and θ, therefore to use the Filtered Backprojection algorithm we must first resample our data into the $r\theta$ domain.

From our simulation we obtain the coordinates of the emitters and detectors. Figure 3.1 a) also gives us emitter/detector pairings. That is we know which detectors are in a particular emitters field of view. These emitter/detector pairings give us the ray sum.

Using this data we are able to resample our simulated data and obtain the values of r, the perpendicular distance from the center of the imaging space to a photon beam (straight line connecting an emitter to a detector), and θ, the angle this line makes with the x-axis. We then take the r and θ values and use them to put the ray sum values on a grid.

For reconstruction (using the Fast Fourier Transform) the data in the $r\theta$ plane
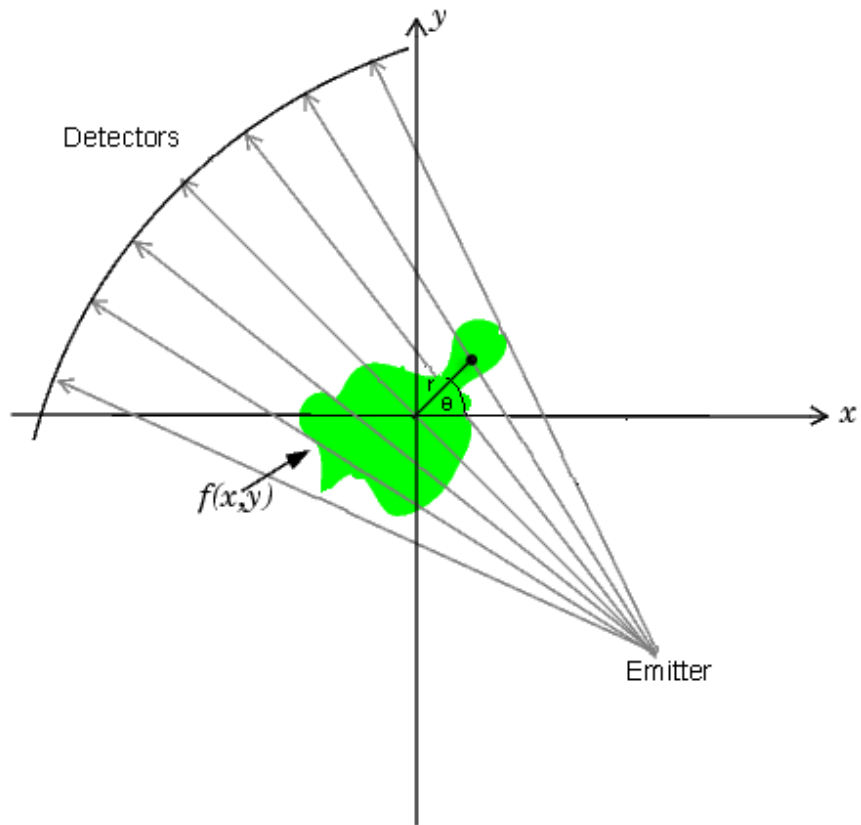
Figure 3.2: The angle each ray makes with r axis and the perpendicular distance r is obtained. r is the perpendicular distance from the center of the imaged space to a photon beam.

Figure 3.3: Data obtained from simulation, projection of the human pelvis.

has to be on a grid. Therefore some of the r and θ values were rounded off. This inevitably causes several X-ray beams to pass along the same path. Therefore we are faced with a choice of replacing already populated regions on the grid based on some criteria, or use the average of the values. We chose the latter option because it makes use of all the data gathered. However, there are more sophisticated methods to populate the grid.

Figure 3.3 is the projection of the pelvis obtained from our simulation. Figure 3.4 shows the resampled simulated data and compares it against the data that would be obtained from a parallel beam scan. As is obvious there is not much difference between the two giving us a promising indication that our resampling method will be able to generate good results.

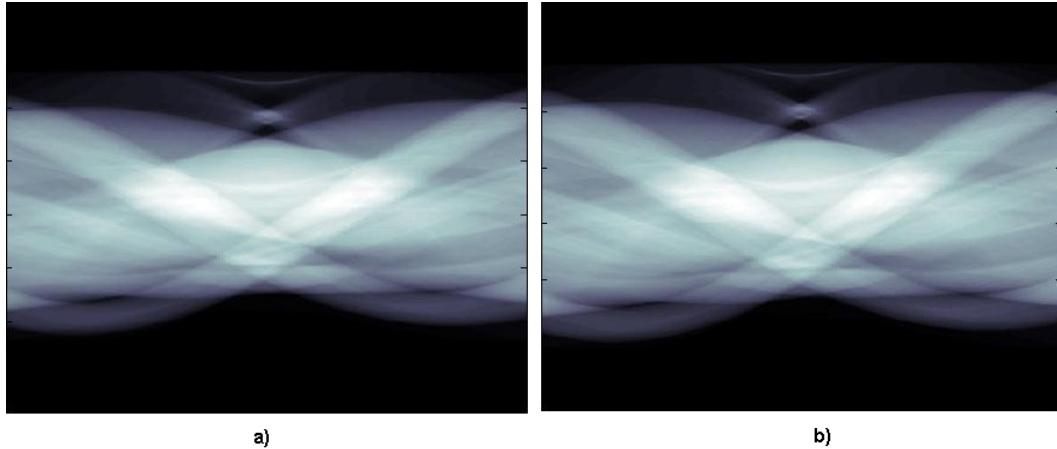We now use the Filtered Backprojection algorithm to reconstruct our image.

Figure 3.4: a) Resampled pelvis projection from our simulator, b) projection obtained from a parallel beam scanner.

3.2 Experiments

In this section we will first describe how our data was obtained. In a later section we will investigate the robustness of our reconstruction method with respect to geometrical perturbations. For example, in our simulation we have perfect knowledge of the position of emitters and detectors. However, in real-life measurements there will always be an error in these readings. We therefore ask the question: how will these errors affect our reconstruction?

We use the Shepp-Logan phantom and a CT slice through the pelvis [31], to test our algorithm. The Shepp-Logan phantom is a standard image used to test the performance of image processing algorithms. The phantom, shown in Fig. 3.5, is composed of ellipses of differing intensitites.. Therefore most of our test cases will be based on the phantom. However, we have also included the pelvis slice as a further test of its efficiency. It should be noted that even under a perfect circular geometry and perfect knowledge of emitter-detector positions, degradation in the form of blurring will occur. This is the result of the fundamental loss of information through the resampling needed to simulate the Radon Transform and

Figure 3.5: The Shepp-Logan phantom.

then the reconstruction.

3.2.1 Data Simulation

In the introduction, we explained that although X-ray images have been obtained from the CNTs, there is still the problem of creating powerful enough photon beams that can penetrate to a significant depth. Therefore, we had to rely on creating simulations of a CNT device to obtain input data. Fortunately the well established Radon Transform allows us to easily simulate a CT projection. Figure 3.6(b) shows a photon beam passing through space along a path described by $r\theta$. The Radon Transform of an image is simply the collection of line integrals for all rays.

Therefore with the knowledge of the position of an emitter and its corresponding detector we can use simple ray casting to approximate the line integral for each ray. We simply sample the image along the line at regular intervals. Thus to approximate the line integral

$$P(i,j) = \int_b^a f_\theta(r_{ij}, \ell)d\ell, \tag{3.1}$$

we use

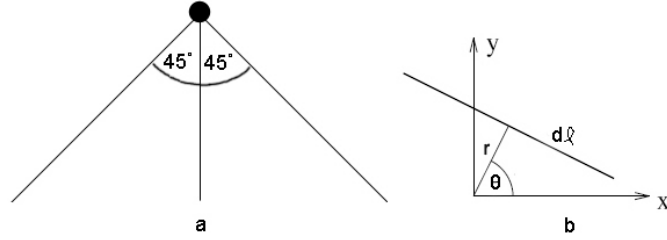$$P(i,j) = \sum_{n=0}^{N} f_\theta(r_{ij}, \ell_n)\Delta\ell. \tag{3.2}$$

Figure 3.6: a) Field of view of emitter, b) The line represents a photon beam, $d\ell$ is a length along the line over which the line integral will be taken.

Now we have to choose positions for our emitters and detectors. As shown in Fig. 3.7 we use a baseline circular geometry with emitters and detectors being placed in alternate positions. A total of 360 emitters and the same number of detectors are positioned at equally spaced intervals.

Each emitter has a direction that indicates the path along which an X-ray beam will pass, and creates an X-ray beam that is fan shaped. Our simulation assumes that each emitter will have a field of view of 45°. Therefore for each emitter we first find which detectors will fall in its field of view and then calculate the line integrals for each pair. The line integrals for a single emitter are stored as one row, as shown in Fig. 3.8.

Generating these line integrals using ray tracing takes $O(\frac{\ell}{\Delta\ell}\alpha NM)$ operations, where $N \times N$ is the size of the image, α is the field of view of an emitter, M is the number of emitters and s is the distance from emitter i to a detector in its field of view.

3.2.2 Irregularity of Geometry

The aim of our experiments is to investigate the performance of our reconstruction method in the presence of irregular geometries. That is we perturb the emitters and detectors from the circular configuration shown in Fig. 3.7(a). We see two general categories of geometrical irregularities: incoherent and coherent. Our experiments
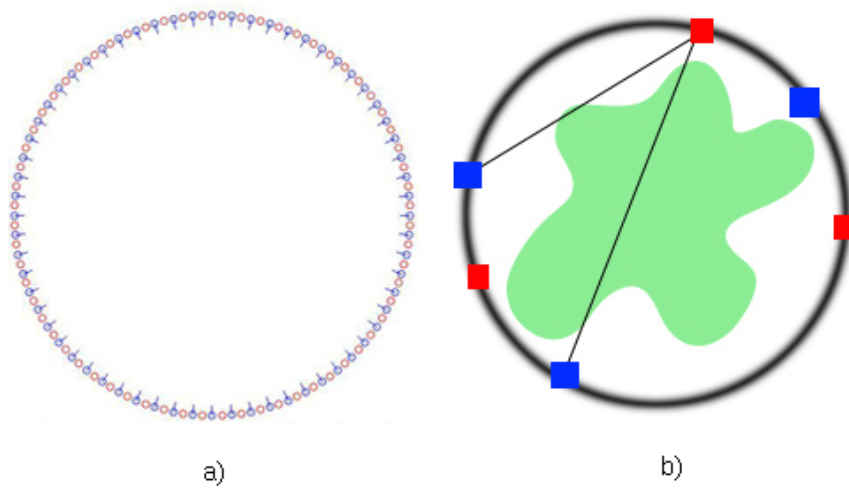
Figure 3.7: a) Emitter detector positions in a circular geometry b) Emitter sending two photon beams to detectors. The blob in the center represents a slice of the object being imaged
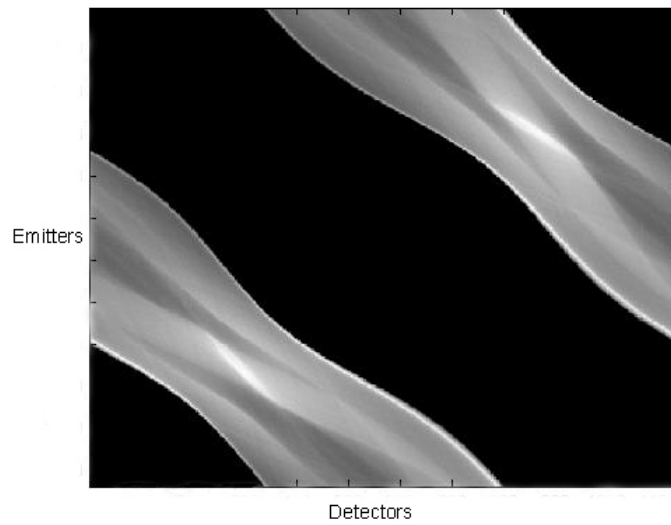

Figure 3.8: Emitter-detector pairs making up the line integrals

will test the performance of our reconstruction method for both types of geometric irregularities.

Additionally, there are two distinct ways in which the irregularity of the geometry affects our reconstruction. In the first case we know the exact positions of the emitters and detectors as they are configured in the irregular geometry. Thus we are able to test our method's ability to correctly use the line integrals to reconstruct a consistent image. The second case uses inaccurate data for the emitter-detector positions, thereby introducing errors that will likely appear in practice. In our experiments we take the known emitters and detector positions and then perturb them to produce these inaccuracies. Reconstruction using these induced errors tests our method's robustness to imperfections in the measurements of emitter and detector positions.

Our experiemnts consist of combinations of these two variables: we call them coherence and accuracy.

Incoherent Irregular Geometry

Thus far our simulation utilizes a circular geometry like that of any CT-scanner. However, the CNTs will be able to be inserted on any sort of flexible material. Thus the geometry will change according to how the material is bent. To simulate some of the different possible aberrations we may expect from a flexible material, we add deformity into the geometry by using Gaussian noise. Matlab provides a function *randn* that generates random variables whose mean is 0 and has a standard deviation, $\sigma = 1$. This function can be easily manipulated to obtain random variables whose mean and standard deviation is user defined. With this function we are then able to easily create an irregular geometry. The process begins by first setting the positions of the emitters and detectors in a circle as shown in Fig. 3.7(a). Then we add Gaussian noise to each of the x and y coordinates of the emitters and detectors positions. Figure 3.9 shows the result of adding Gaussian noise where the standard deviation is 0.5.
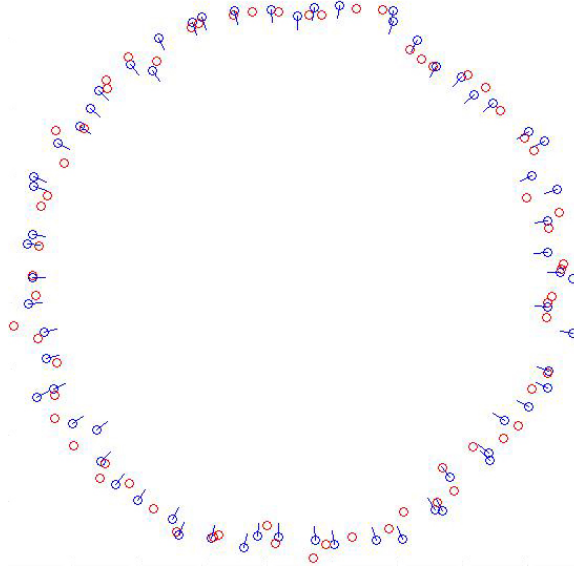
41

Figure 3.9: Emitter/detector positions in an incoherent geometry, $\sigma = 0.5$

Coherent Irregular Geometry

In the incoherent irregular geometry there can be some significant warping of the emitter and detector positions as shown in Fig. 3.9. In this case we have emitters and detectors whose positions are so warped that it appears as if they are floating in free space and not actually attached to anything. However, if attached to some fabric then this kind of radical aberration will not form. As in the previous section, we first position the emitters and detectors in a circle. We then displace the emitter and detectors by pertubring the x and y coordinates with a trigonometric function. The amplitude gives the degree of irregularity of the geometry. Higher amplitude results in a greater pertubation from the circular geometry, and hence a more irregular geometry. However, unlike the case of the incoherent irregularity we do not allow the emitters to move randomly and thereby interchange positions. All emitters and detectors in a neighbourhood move in the same general direction while at the same time being perturbed to different degrees. Figure 3.10 shows the resutls of warping the positions of emitters and detectors by an amplitude of 0.5.
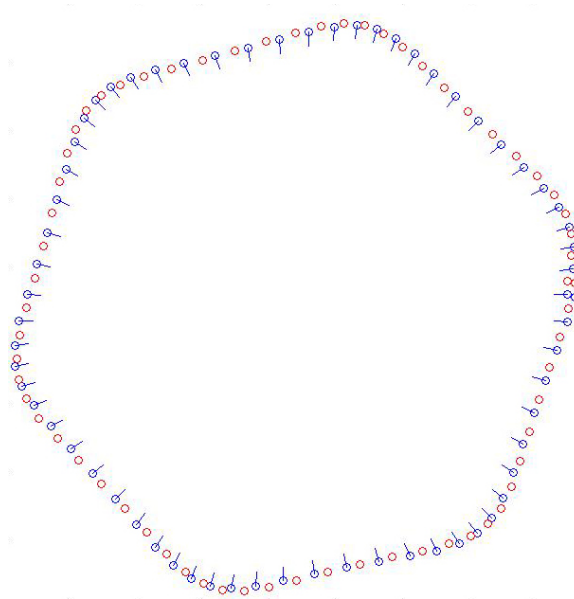
42

Figure 3.10: Emitter/detector positions in a coherent geometry, amplitude $= 0.5$

3.2.3   Errors in Emitter and Detector Positions

In many of our experiments, we assume that the positions of the emitters and detectors are known. However, in the real world such precision is difficult to obtain. We therefore decided to include errors in the values of the emitter and detector positions which would in turn create incorrect data for the pre-processing step. That is, there will be errors in the emitter-detector pairings that translate into errors in the calculated $r\theta$ coordinates. Like the case of irregularity of geometry, there are two ways by which we include inaccuracies. The first method uses a Gaussian distribution to create incoherent positional errors. The second method uses trigonometric functions to create a more coherent positional error. These two types of inaccuracies provide a very good test for the robustness of our reconstruction algorithm. Brief descriptions of how these errors are implemented are given below.

Incoherent Errors

We use Gaussian noise to create inaccuracies in our knowledge of the emitter and detector positions. As in the case of the irregular geometry this noise creates a 'random' error in the data. To obtain these inaccuracies, we first use our simulation to create data and store the line integral values and the positions of the emitters and detectors. The irregular geometry can be of either type. Taking the coordinates of each emitter and detector we apply Gaussian noise to perturb the positions. The magnitude of the inaccuracy depends on the standard deviation of the Gaussian. With errors introduced, the emitter-detector pairs and $r\theta$ values have to be re-calculated. This is because the pairs obtained in the original simulation will be invalid after the introduction of the inaccuracies. The data set containing the new emitter-detector pairs and the original line integrals are then used to reconstruct the image. Chapter 4 gives the results of the reconstructions.

Coherent Errors

The second type of inaccuracy introduced is one that takes a more coherent shape. Unlike those errors produced by using Gaussian noise, the emitters and detectors positions are changed such that they agree with their neighbors. As in the case of a coherently irregular geometry, we use a trigonometric function. The amplitude of the function gives the degree of error. Similar to the creation of incoherent errors we first use our simulation to generate the line integral values, and collect the emitter and detector positions. Each emitter and detector position is then rendered 'inaccurate' using the trigonometric function. New emitter-detector pairs and $r\theta$ values are computed. Together with the line integrals we can then reconstruct our image. Chapter 4 gives the results of the reconstructions.

Chapter 4

Results and Discussion

In this chapter we show the results of our reconstruction algorithm. We predominantly use the Shepp-Logan phantom, as it is the standard, to test our reconstructions. The Normalized Root Mean Square Error (normalized RMSE) is used to provide a quality measure of our reconstruction algorithm, and is given by,

$$E^2 = \frac{\sum \mid g(x,y) - f(x,y) \mid^2}{\sum \mid f(x,y) \mid^2}, \tag{4.1}$$

where $g(x,y)$ is the reconstructed image and $f(x,y)$ is the phantom test image. The result, E^2, is the normalized mean-square error and E is therefore the normalized root-mean-square error [32]. This error metric will be used throughout to check our reconstruction. Furthermore the Ram-Lak filter is used throughout in the filtered backprojection algorithm. However, it is not enough to say that our reconstruction has an RMSE of some value. Such a result is all too vague and we must therefore compare it against a standard. The standard we have taken is Matlab's *ifanbeam* function. The fanbeam geometry is the closest geometry to that defined by our simulation, since each emitter has a fan shape beam. We therefore calculate the RMSE of the ifanbeam function on the phantom and use that as our basis. The function is applied to a perfectly circular geometry and a phantom projection obtained by Matlab's *fanbeam* projection.

4.1 Irregularity of Geometry

We first test how our algorithm performs with irregular geometry.

4.1.1 Incoherent Irregularity

Standard Deviation σ	Normalized RMSE (Ram-Lak Filter)	Normalized RMSE (Hamming Filter)
ifanbeam	0.4000	0.3516
0.0	0.4904	0.4724
0.1	0.4889	0.4721
0.3	0.4902	0.4721
0.5	0.4907	0.4735
0.7	0.4957	0.4728
1.0	0.5084	0.4744

Table 4.1: The Root-mean-squared errors of the reconstructed Shepp-Logan phantom in an incoherent irregular geometry scanner.

In Table 4.1 we compare the quality of the reconstructed image using the Ram-Lak filter and the Hamming filter. The Ram-Lak filter, described earlier, is a high pass filter and therefore is sensitive to noise. However, the Hamming filter is formed by multiplying the Ram-Lak filter by a window. This results in deemphasizing high frequencies [27]. Hence we are not limited by the filter and investigation into custom filters may improve the quality even more.

Note that with perfectly circular geometry ($\sigma = 0$), our error is nonzero. This is the baseline reconstruction error for this resolution. All other reconstruction errors should be interpreted relative to this baseline error.

Figure 4.1 shows the reconstruction, under the Ram-Lak filter, at different degrees of perturbations. As seen from Table 4.1 and confirmed by Fig. 4.1, the quality of the image deteriorates slightly with high perturbation. However, even in

our highest degree of irregularity, the major features of the phantom are still discernable. To put this into perspective, irregularity of $\sigma = 1.0$ is akin to wrapping a material around an object and then taking part of the material and twisting it. Such perturbations will maker some of the emitters and detectors redundant, while possibly undersampling along some ray lines (leading to an undersampled region in the $r\theta$ plane). However, we are still able to discern features with ease.
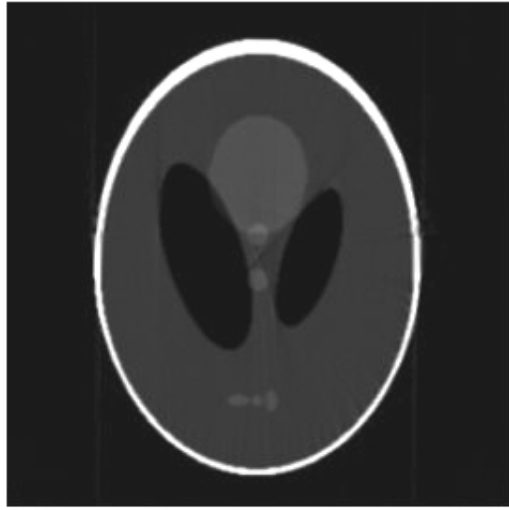
4.1.2 Coherent Irregularity

| Amplitude of error α	Normalized RMSE Pelvis (Ram-Lak Filter)	Normalized RMSE Phantom (Ram-Lak Filter)
ifanbeam		0.4000
0.0	0.1972	0.4904
0.1	0.1978	0.4908
0.3	0.1996	0.4906
0.5	0.1991	0.4923
0.7	0.2102	0.4944
0.9	0.2179	0.4987
1.0	0.2223	0.5024

Table 4.2: The Root-mean-squared errors of the reconstructed Pelvis in an Coherent irregular geometry scanner.

Table 4.2 shows the RMSEs obtained using a projection of the pelvis and the phantom. The error in the pelvis is much lower because its material generally has a more consistent absorption coefficients than those assigned to the phantom. Therefore the interpolations carried out in the reconstruction and resampling processes will be more consistent. While in the phantom the more varied coefficients will result in larger errors accumulated through reconstruction. Figures 4.2 and 4.3 show the reconstructions of the phantom and pelvis respectively.
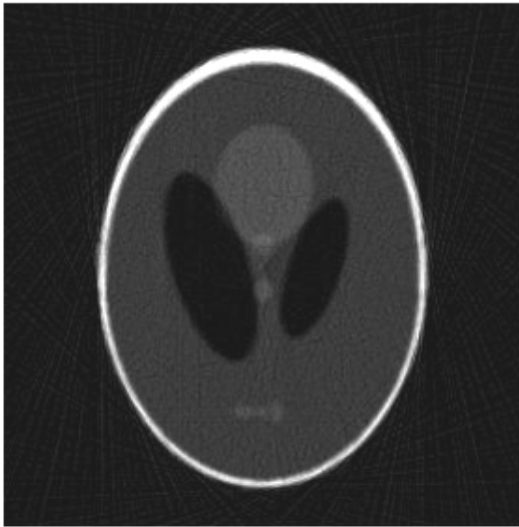
As expected a coherently irregular geometry will perform better than its in-
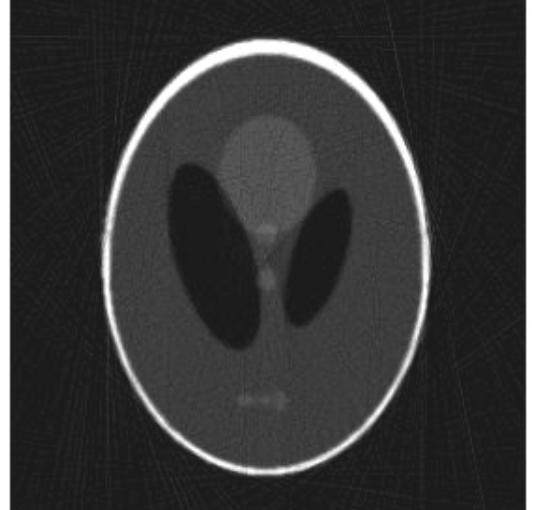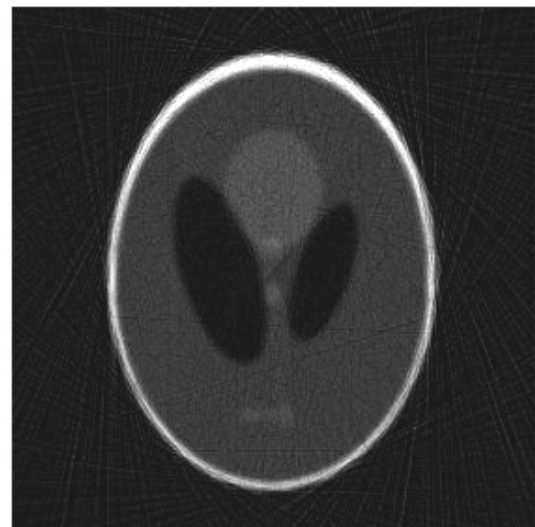
Figure 4.1: Reconstruction of Shepp-Logan Phantom with an incoherency in the irregularity of the geometry, σ. a) $\sigma = 0.0$, b) $\sigma = 0.5$, c) $\sigma = 0.7$, d) $\sigma = 1.0$

coherent counterpart. From Tables 4.1 and 4.2 we see that in the case of the incoherent irregularity the RMSE value dips and then rapidly increases, while that of the coherent irregularity increases gradually. It is observed that for a few cases the RMSE value of the incoherent irregularity is actually a little smaller than that of coherent. However, this difference is quite negligible and in such situations we compare the reconstructed images to obtain a better conclusion.

Figure 4.4 gives us an idea of what effect the type of irregularity in geometry contributes. As is seen in the Fig. 4.4 a) there are many more oscilation artifacts than in b), supporting our conclusion that the coherently irregular geometry will give a better reconstruction, as they are fewer obvious artifacts.

4.2   Errors in Positions of Emitters and Detectors

In this section we look at the results of our reconstruction when the positions of the emitters and detectors contain some degree of error. We test our reconstruction method by introducing emitter/detector position errors to a variety of different geometrical scenarios: regular (circular) geometry, incoherent irregular geometry and coherent irregular geometry. We limit the number of tests, but at the same time we want to test on a sufficiently irregular geometry. We decided to use irregularities of standard degree or amplitude (depending on the type of irregularity) of 0.5. We believe a higher degree of irregularity would not be very practical in real situations. It is quite likely that many cases would actually have lower degrees if irregularity.

4.2.1   Incoherent Errors

Table 4.3 shows the RMSE obtained by the pelvis and phantom reconstructions with a coherent irregularity and various degrees of incoherent poistional errors. The inaccuracy in the positions of emitters and detectors is obtained using Gaussian noise, as described in the previous chapter. Figure 4.5 shows the reconstruction under varied degrees of inaccuracy.
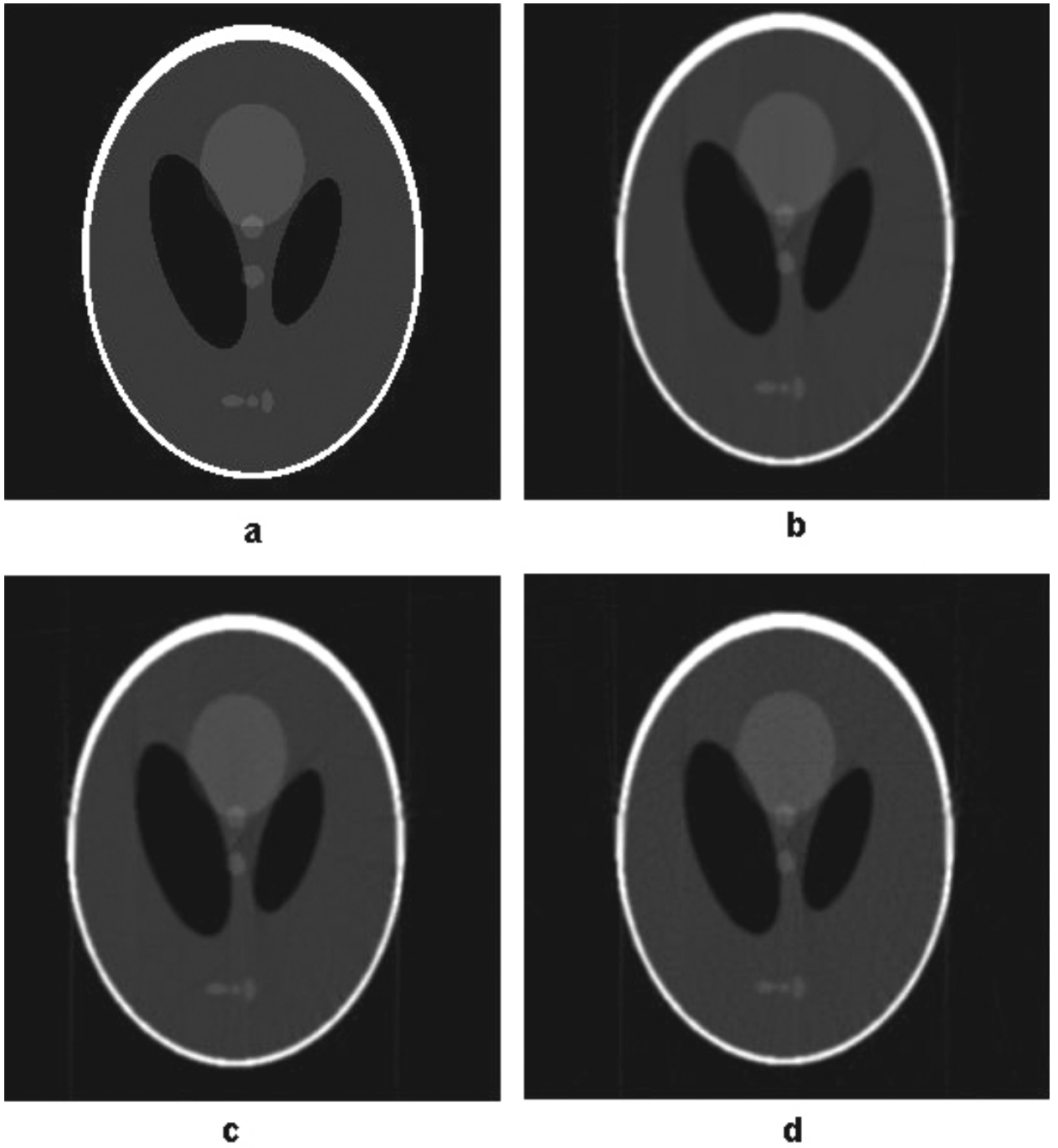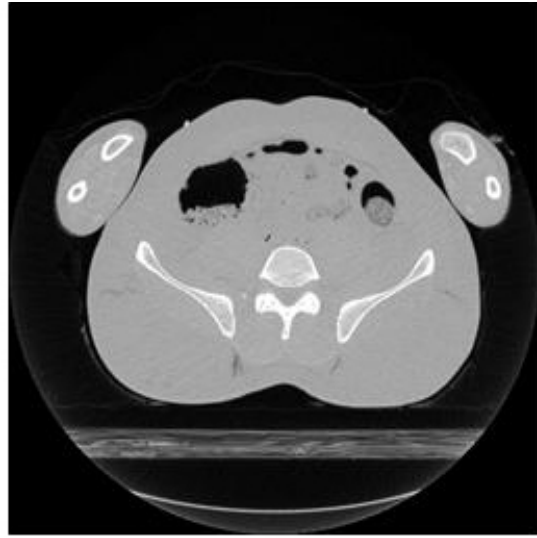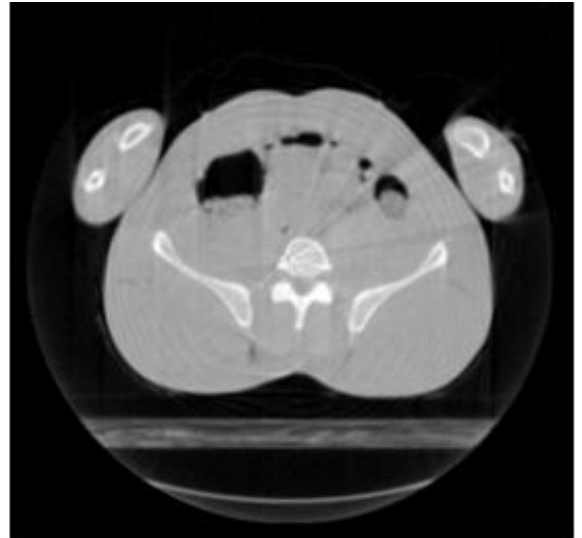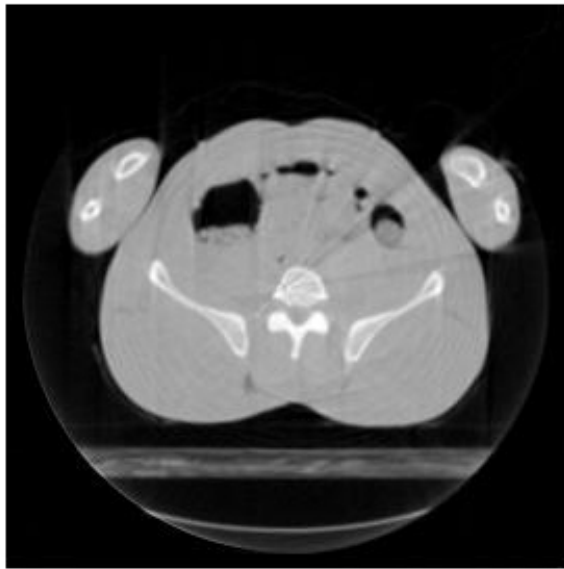
Figure 4.2: Reconstruction of Phantom with a coherency in the irregularity of the geometry, α. a) Original Phantom, b) $\alpha = 0.1$, c) $\alpha = 0.5$, d) $\alpha = 0.9$

Figure 4.3: Reconstruction of Pelvis with a coherency in the irregularity of the geometry. a) Original Pelvis slice, b) $\alpha = 0.1$, c) $\alpha = 0.5$, d) $\alpha = 0.9$

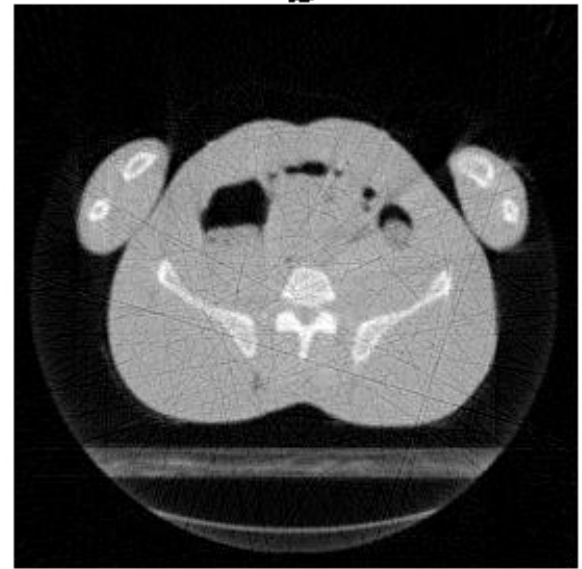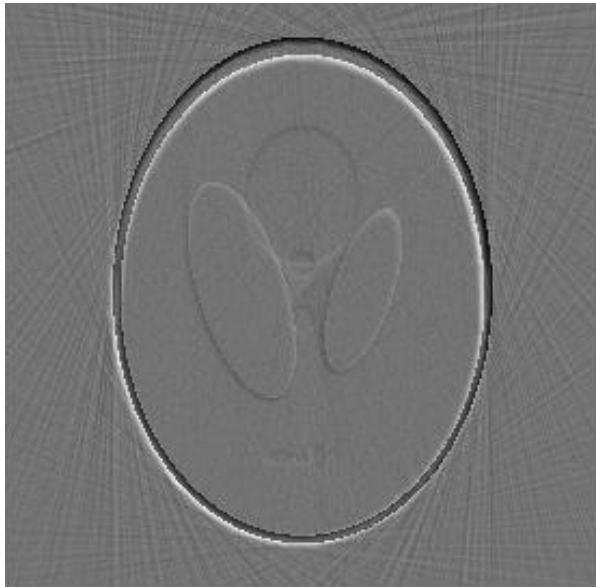Figure 4.4: a) The difference image between the phantom and reconstruction under an incoherent irregular geometry of $\sigma = 0.7$, b) the difference image between the phantom and reconstruction under a coherent irregular geometry of $\alpha = 0.7$.

Standard Deviation σ	Normalized RMSE (Ram-Lak Filter)
ifanbeam	0.4000
0.0	0.4904
0.1	0.4901
0.3	0.4902
0.5	0.4906
0.7	0.4950
1.0	0.4983

Table 4.3: The Root-mean-squared errors of the reconstructed Shepp-Logan phantom with Gaussian induced positional inaccuracies of emitters and detectors.

Amplitude α	Normalized RMSE (Ram-Lak Filter)
ifanbeam	0.4000
0.0	0.4904
0.1	0.4903
0.3	0.4904
0.5	0.4912
0.7	0.4919
1.0	0.4948

Table 4.4: The Root-mean-squared errors of the reconstructed Shepp-Logan phantom with a coherently induced positional inaccuracies of emitters and detectors.

From the tables we see that even with large inaccuracies in emitter/detectors positions the quality of the reconstructed image does not deteriorate as severely as in the case of irregular geometry. However, as the magnitude of the error increases the quality of the reconstruction falls. But Figs. 4.5 and 4.6 we are able to easily pick out the different objects, though there is a discernable increase in artifacts. Given

the results and those obtained from irregular geometries we see that the induced inaccuracies do not affect our reconstruction on the same magnitude as geometric irregularity.

Standard Deviation σ	Normalized RMSE (Pelvis Coherent Geometry (0.5))	Normalized RMSE (Shepp-Logan Phantom) Coherent Geometry(0.5)
0.1	0.1994	0.4907
0.2	0.2019	0.4918
0.3	0.2075	0.4945
0.5	0.2146	0.4960
0.7	0.2224	0.4963
1.0	0.2311	0.5020

Table 4.5: The RMSE of the reconstructed Pelvis slice and Shepp-Logan phantom, where we use a coherent irregular geometry of amplitude 0.5.

Table 4.5 shows the RMSE obtained by the pelvis and phantom reconstructions with a coherent irregularity and various degrees of incoherent poistional errors. Figure 4.7 shows the reconstruction under varied degrees of inaccuracy.

Table 4.6 gives the RMSEs under the introduction of the Gaussian based inaccuracies on incoherent geometry. As is expected the RMSE observed in the coherent cases are smaller than in the incoherent. This is primarily due to the fact that in the case of inaccuracy of 0, the incoherent geometry has a larger RMSE. This propagates as we add inaccuracies in the positions of emitters and detectors. Figures 4.8 and 4.9 show the reconstruction of the phantom and pelvis respectively. We see there are more artifacts observed in the case of incoherent geometry. In the incoherent geometry we already have a chaotic distribution of the emitters and detectors. Adding more Gaussian noise will make the distribution even more chaotic resulting in the artifacts. These artifacts are the result of undersampling of the data. A less evenly distributed configuration will result in many regions where undersampling occurs.
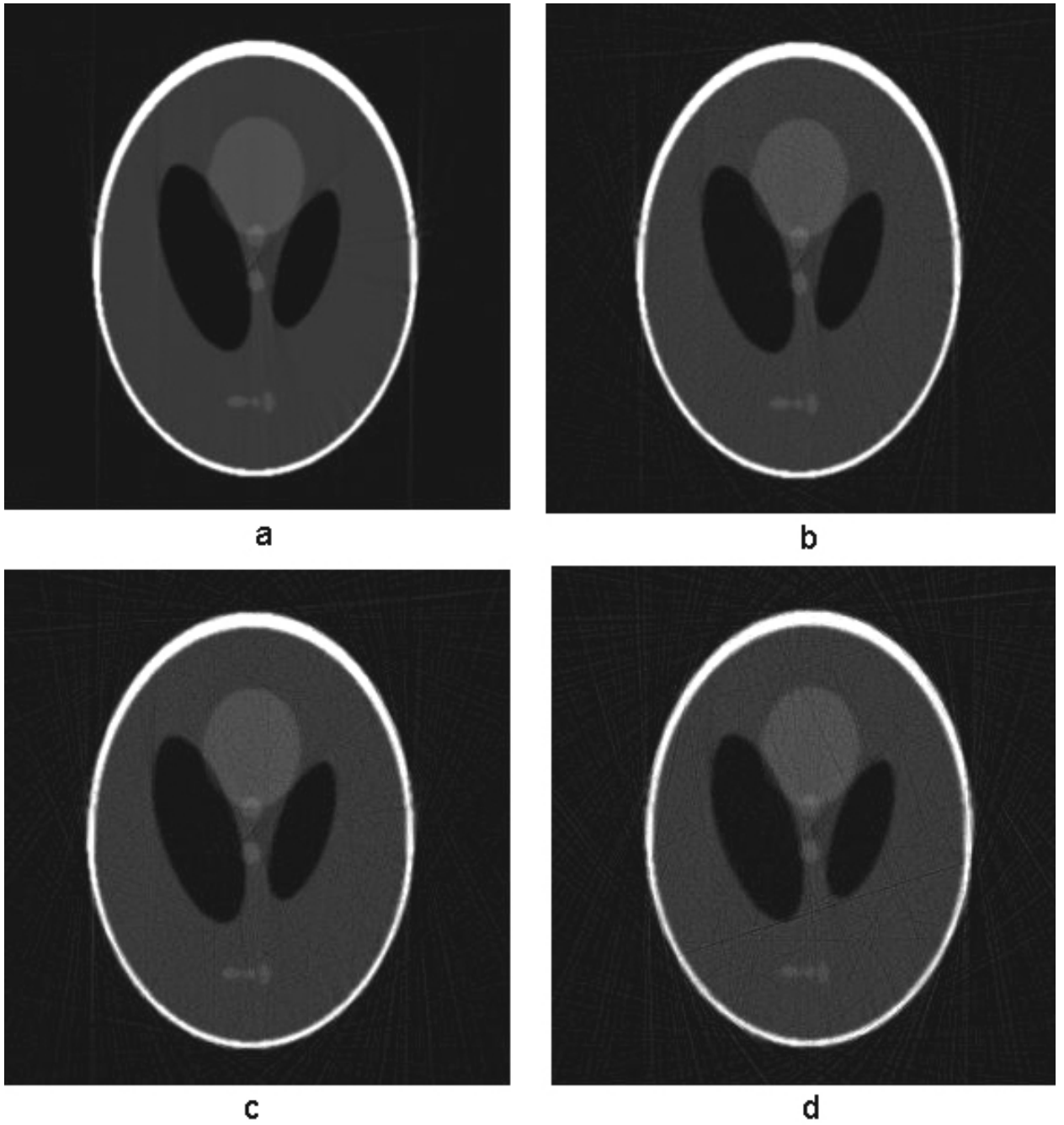
Figure 4.5: Reconstruction of Shepp-Logan Phantom with an incoherent error in recorded emitter detector positions. A regular geometry is used. a) $\sigma = 0.1$, b) $\sigma = 0.5$, c) $\sigma = 0.7$, d) $\sigma = 1.0$

Figure 4.6: Reconstruction of Shepp-Logan Phantom with a coherent error in recorded emitter detector positions. A regular geometry is used. a) $\sigma = 0.1$, b) $\sigma = 0.5$, c) $\sigma = 0.7$, d) $\sigma = 1.0$

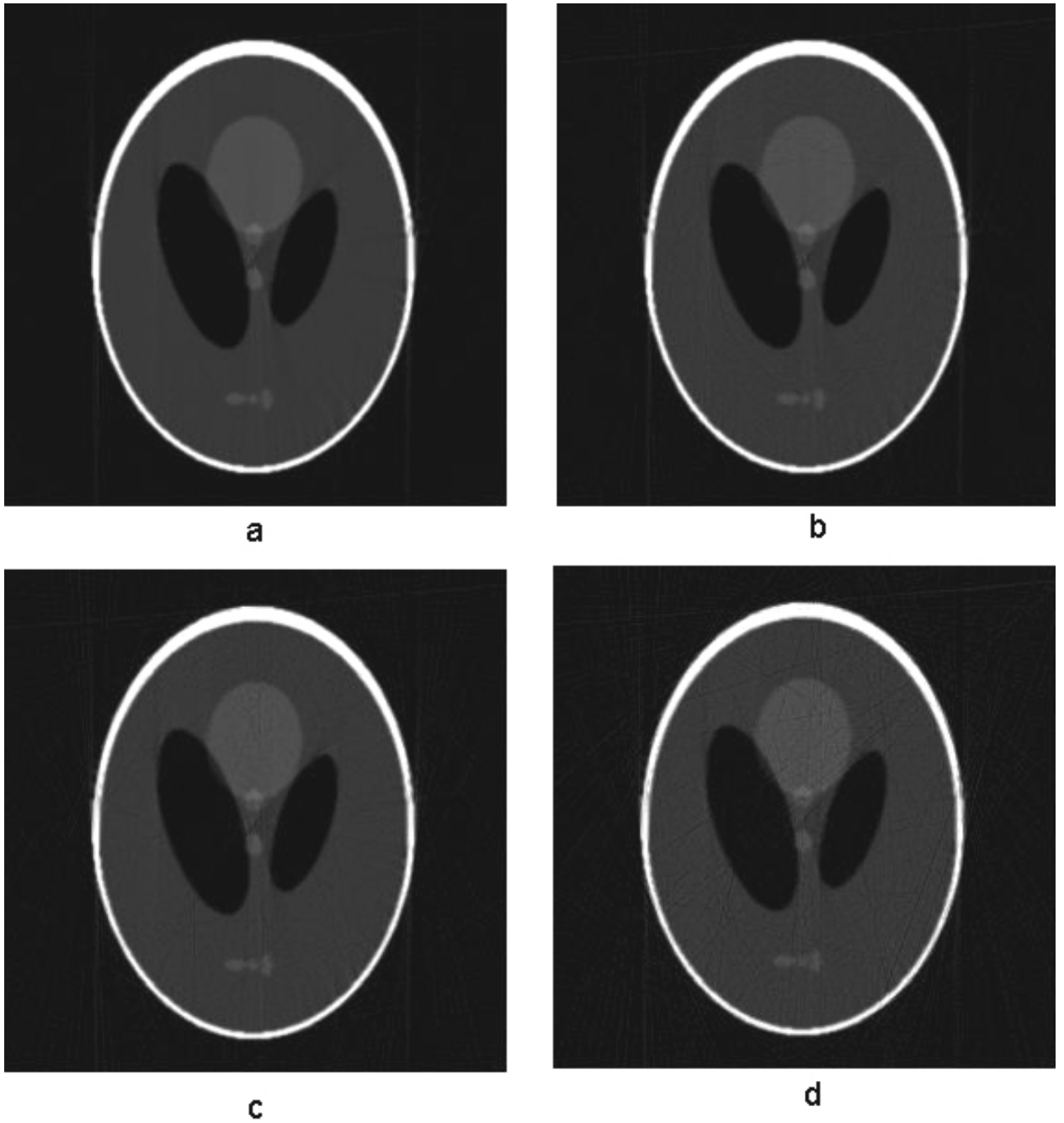Figure 4.7: Reconstruction of Shepp-Logan Phantom with an incoherent error in recorded emitter detector positions. Coherency in the irregularity of the geometry is $\alpha = 0.5$. a) $\sigma = 0.1$, b) $\sigma = 0.5$, c) $\sigma = 0.7$, d) $\sigma = 1.0$
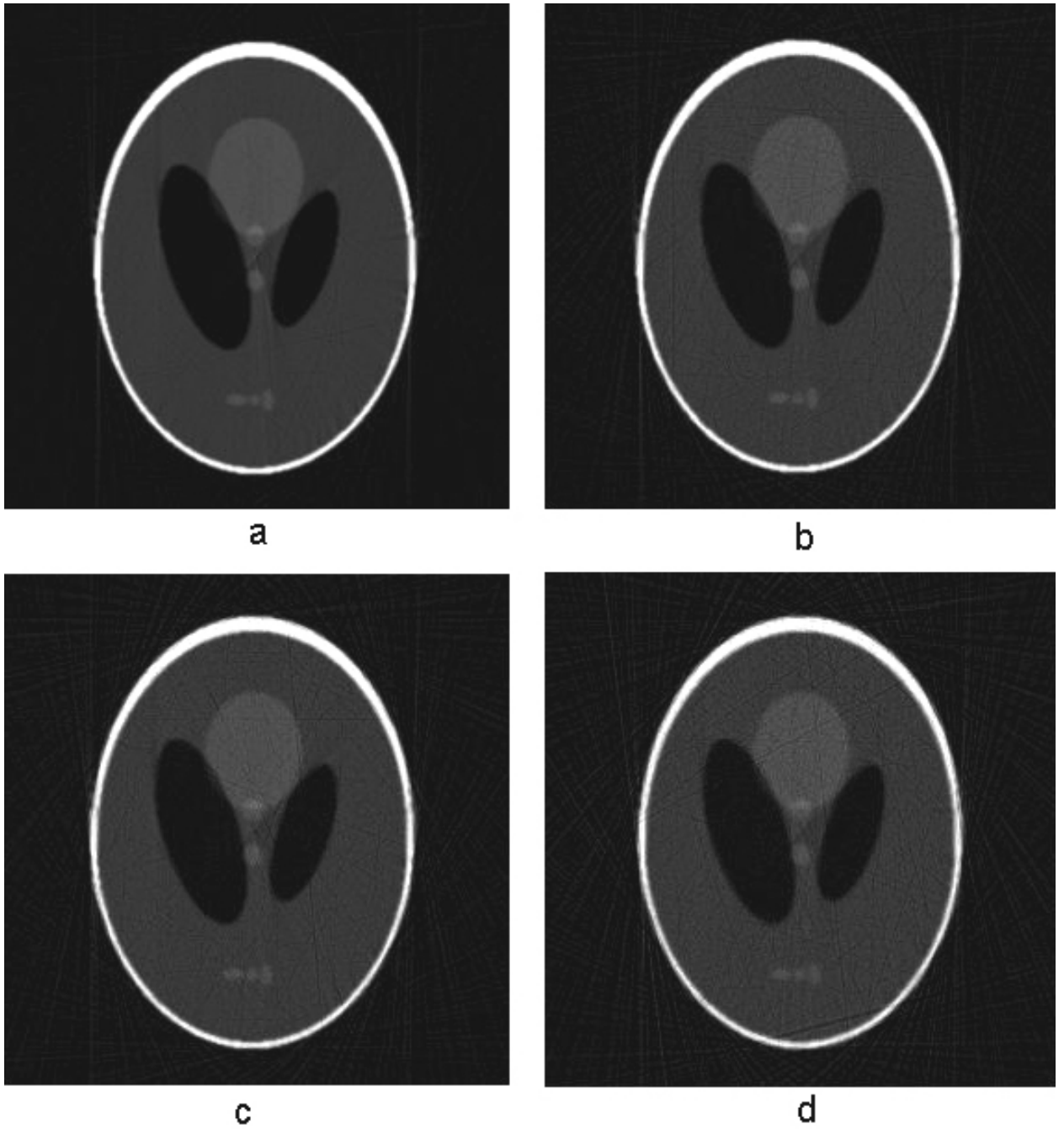
Figure 4.8: Reconstruction of Shepp-Logan Phantom with an incoherent error in recorded emitter detector positions. Incoherency in the irregularity of the geometry is 0.5. a) $\sigma = 0.1$, b) $\sigma = 0.5$, c) $\sigma = 0.7$, d) $\sigma = 1.0$

Figure 4.9: Reconstruction of Pelvis with an incoherent error in recorded emitter detector positions. Incoherency in the irregularity of the geometry is 0.5. a) $\sigma = 0.1$, b) $\sigma = 0.5$, c) $\sigma = 0.7$, d) $\sigma = 1.0$

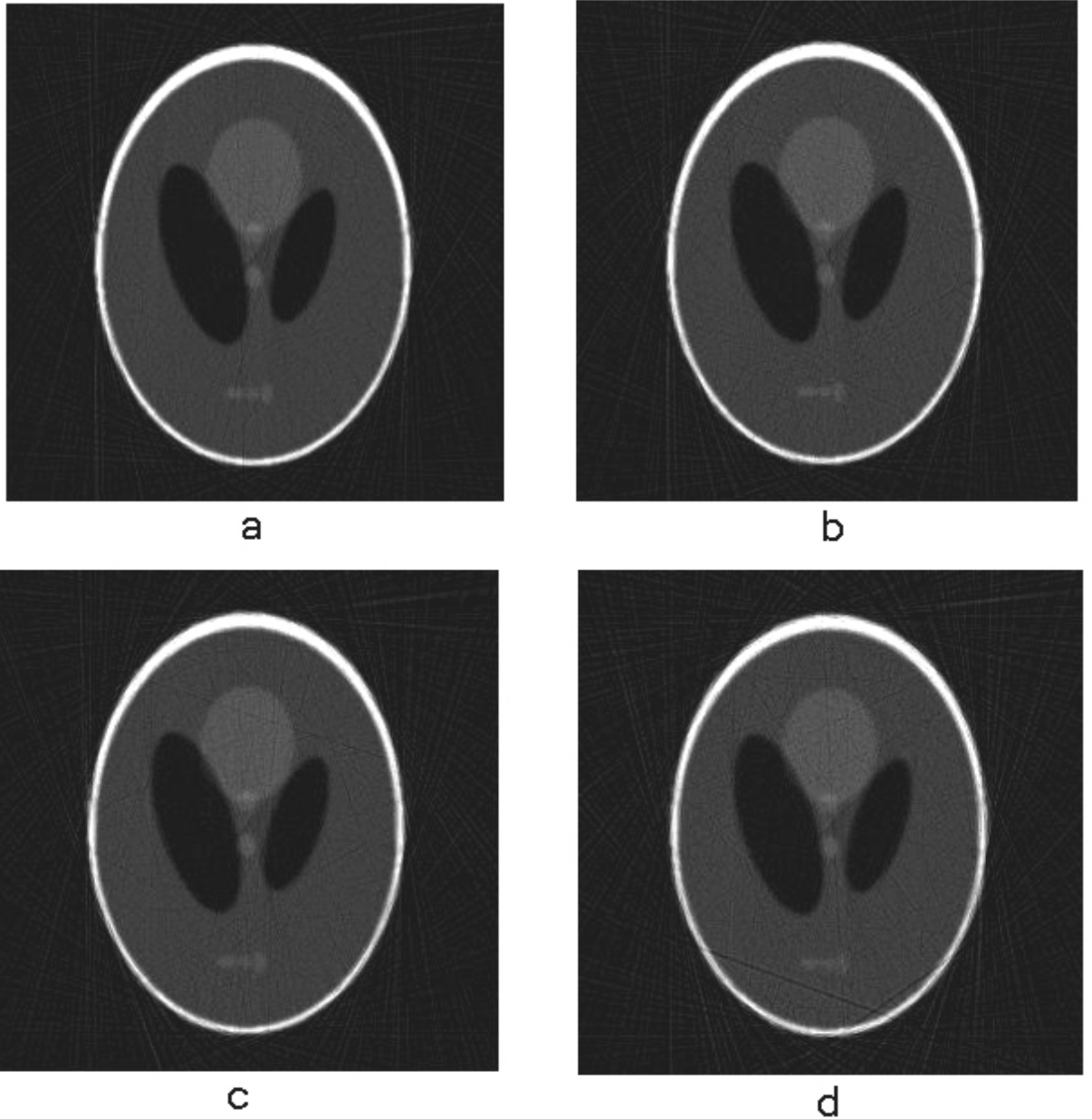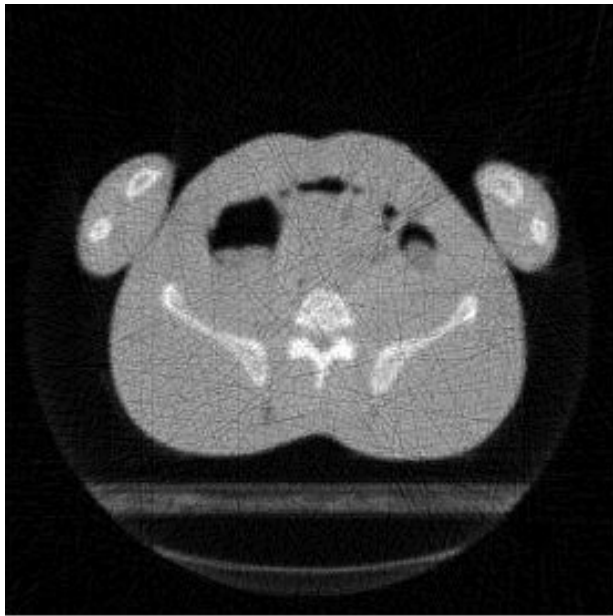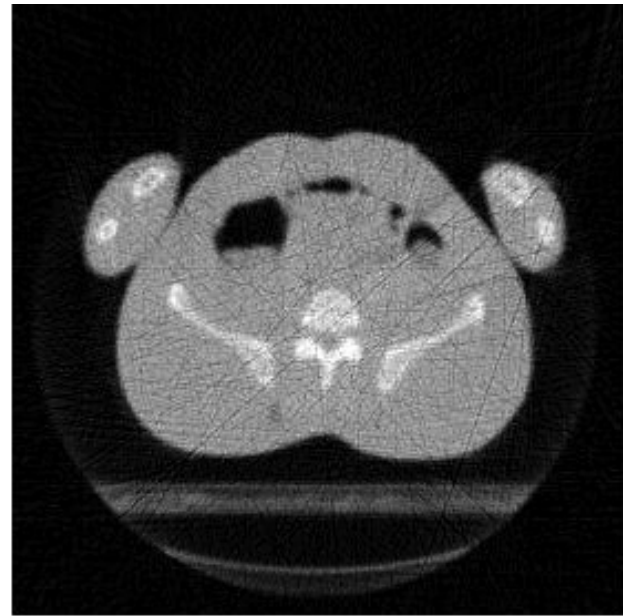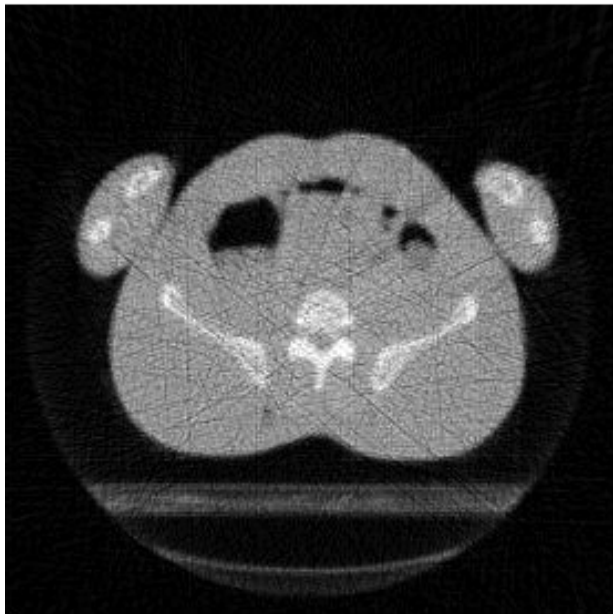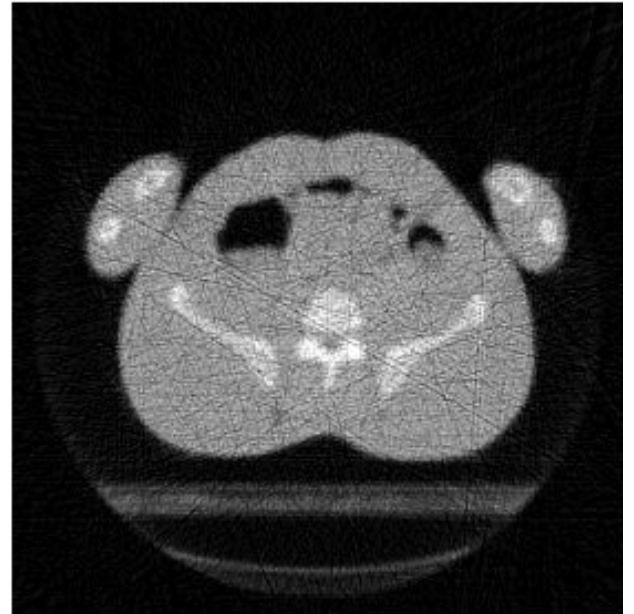| Standard Deviation σ	Normalized RMSE (Pelvis Incoherent Geometry (0.5))	Normalized RMSE (Shepp-Logan Phantom) Incoherent Geometry(0.5)
0.1	0.2187	0.4920
0.2	0.2209	0.4907
0.3	0.2232	0.4954
0.5	0.2277	0.4973
0.7	0.2320	0.4939
1.0	0.2471	0.5044

Table 4.6: The RMSE of the reconstructed Pelvis slice and Shepp-Logan phantom, where we use a incoherent irregular geometry of standard deviation 0.5. The errors are created using Gaussian noise with different standard deviations.

4.2.2 Coherent Errors

Amplitude of error α	Normalized RMSE (Shepp-Logan Phantom) Coherent Geometry (0.5))	Normalized RMSE (Shepp-Logan Phantom) Incoherent Geometry(0.5)
0.1	0.4729	0.4701
0.2	0.4729	0.4691
0.3	0.4730	0.4696
0.5	0.4728	0.4696
0.7	0.4728	0.4696
1.0	0.4728	0.4714
2.0	0.5104	0.4906

Table 4.7: The RMSE of the reconstruction (Shepp-Logan phantom) with coherent errors in the emitter-detector positions. We use both a coherent irrgular geometry and an incoherent one. In both case the irregularity is given by α or $\sigma = 0.5$

Table 4.7 shows the RMSEs obtained using a trigonometric function to obtain inaccuracies. As explained in the previous chapter, using a trigonometric function will result in a more coherent distribution of data. The RMSE values in Table 4.7 are much smaller than those produced by the Gaussian inaccuracy (shown in Tables 4.5 and 4.6). This is because the trigonometric function does not cause the device to move around chaotically and this more consistent movement results in better reconstructions. Figures 4.10 and 4.11 show the reconstructions of coherent inaccuracy in both coherent and incoherent geometries respectively. We see that there are fewer artifacts than in the case of the incoherent inaccuracies. The reconstruction also produces better contrast. As in the case of the geometries we believe that these characteristics are a result of better sampling.

Table 4.7, however, shows a lower RMSE for the incoherent geometry than the coherent one. But Fig. 4.10 shows better reconstruction for the coherent geometry. This contradiction is not clearly understood, but the better results shown in Fig. 4.10 are expected. In Table 4.7 we see that the RMSE for the coherent irregularity changes slowly. Visually examining the reconstructions, 0.5 and 1.0 in Fig. 4.10, shows that there are more oscillation artifacts. To be sure, Table 4.7 shows that in the case of an error of amplitude 2.0 a much larger RMSE results.

Figure 4.10: Reconstruction of phantom with a coherent error in recorded emitter detector positions. Coherency in the irregularity of the geometry is 0.5. a) $\alpha = 0.1$, b) $\alpha = 0.5$, c) $\alpha = 0.7$, d) $\alpha = 1.0$
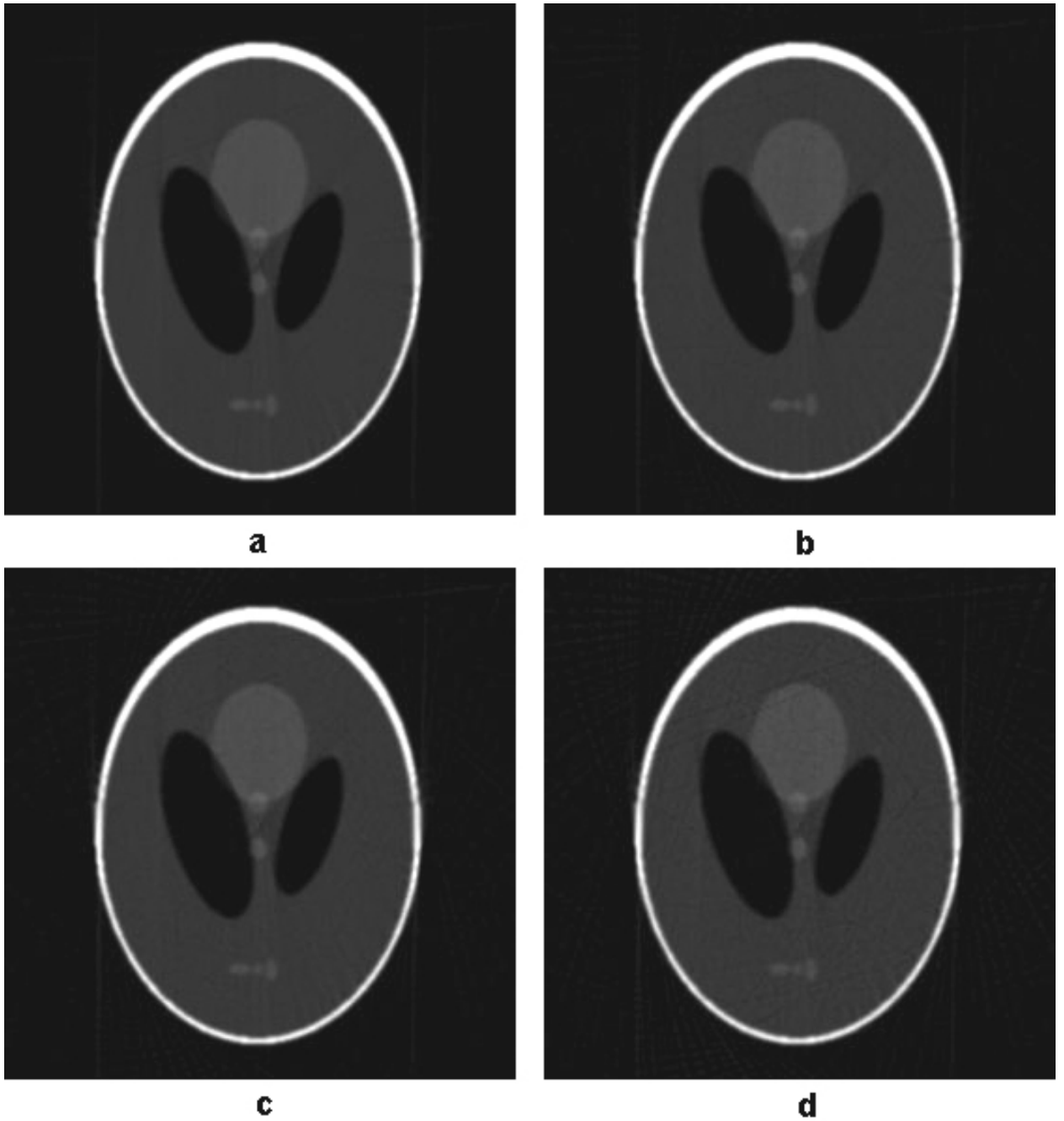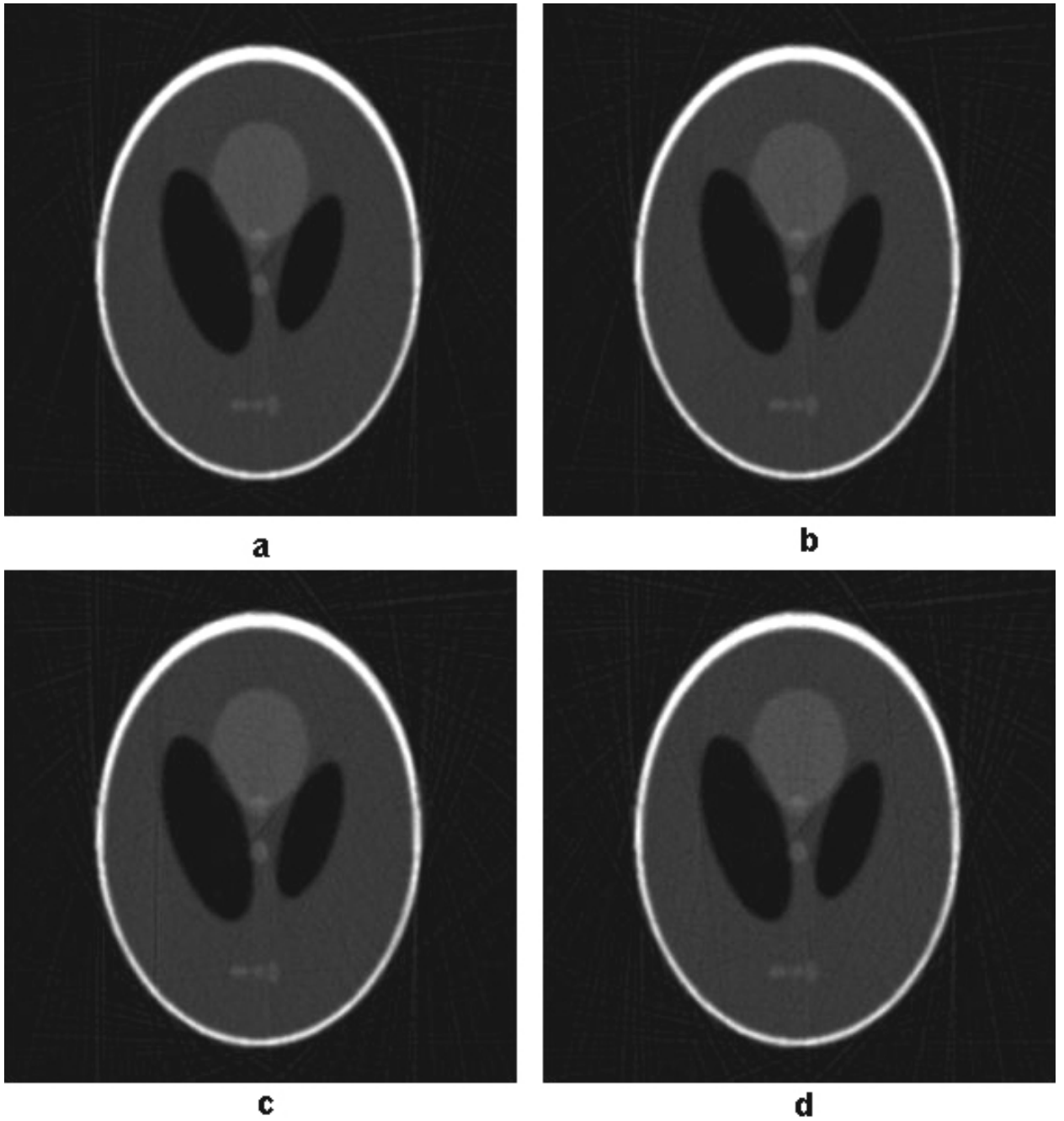
Figure 4.11: Reconstruction of phantom with a coherent error in recorded emitter detector positions. Incoherency in the irregularity of the geometry is 0.5. a) $\alpha = 0.1$, b) $\alpha = 0.5$, c) $\alpha = 0.7$, d) $\alpha = 1.0$

Chapter 5

Conclusions and Future Work

5.1   Conclusions

The General Geometry CT Reconstruction algorithm generally yields very good reconstructions. Many of the artifacts found in the reconstructions are believed to be the result of inconsistent sampling (undersampling, or contradictory redundant samples) of ray sums that are tangent to high-contrast edges in the image. Increasing the number of emitters and detectors should improve the quality. It is interesting to observe that reconstruction under coherent irregular geometry results in a better image than that derived from an incoherent geometry. Although there are a few cases where RMSE is smaller for the incoherent geometry, the reconstructed images suggest a different result. For example in the reconstructions of a coherent geometry (Fig. 4.2) and incoherent (Fig. 4.1) we see sharper images in the case of a coherent geometry. The line artifacts observed in the 'incoherent' results are more pronounced. Furthermore as the irregularity of the geometry increases we observe that the RMSEs of the incoherent geometry increases more rapidly than its coherent counterpart.

In the case of the incoherent geometry, where emitters and detectors are displaced independently, there is the likelihood that they may bunch up. In such an event there will be regions of $r\theta$ space that will be undersampled. With portions

of the region unsampled the resampling will result in errors. These errors will then propagate across the reconstruction. The 'bunching up' effect is the major difference between the incoherent and coherent geometries. However, it should be noted that in a real device, emitters and detectors are attached to the same material. Therfore it is not very likely for high levels of incoherency to occur. Though the fact that our algorithm is able to perform well under even such improbably geometrie does provide us with evidence of its robusteness.

We have also included a slice of the pelvis to be reconstructed under a coherently irregular geometry (see Fig. 4.3). The reconstructions have been satisfactory, however, a large number of artifacts interweave the surface. This result does not occur in the phantom, and further work should be conducted to research this result.

We have also included errors in the recorded positions of our emitters and detectors. This allows us to see how robust our algorithm is in 'real world' situations. There are many devices that can retrieve positions in space. However, none has shown itself to be completely accurate. Even with this constraint, our algorithm deals with very large 'inacccuracies' satisfactorily and therefore the inherent lack of precision of such devices will be more of a nuisance than a major issue.

5.2 Future Work

Our algorithm only deals with a slice of an object. However, in most practical cases we will want volume imaging. Again we look at work that has been done before. The fan beam scanner provides a good geometric similarity for a three-dimensional case. The filtered backprojection algorithm can again be used in this case, and resampling of the data will also be necessary [27]. We believe that our method can be generalized easily to volume imaging.

We see that the filter function used in the reconstruction affects the quality of the image produced. In the majority of our reconstructions we have used the Ram-Lak filter. However, the Ram-Lak filter is a high pass filter and therefore sensitive to noise. Other filters such as the Shepp-Logan or Hamming filters, such

as the Shepp-Logan or Hamming filters, should be investigated [27]. Work can also be done on creating a specific filter to match our needs.

The simulation of the input data did not take into consideration the effects of scattering of X-ray photons within the body. Therefore for future work we will incorporate the effects of scattering into the simulation and test our reconstruction algorithm on this new data.

The detectors have nonlinearities, such that they have differential sensitivities as a function of angle of incidence and curvature. These factors should be incorporated into our simulation.

Our errors were created in a rather ad-hoc fashion. However, it is likely that different forms or patterns of positional errors will produce different results. We have shown that incoherent inaccuracies and a particular form of coherent inaccuracy give different artifacts. How these artifacts change with varying accuracy and with the overall geometry still needs to be investigated in more depth. Therefore further work into devices that record positions in three-dimensional space, and how the errors in measurements are propagated, should prove useful.

Our resampling method uses a simple averaging technique to populate the $r\theta$ space. However, more complex resampling methods, like Delaunay triangulation, should be investigated. Matlab uses the Delaunay triangulation in its *griddata* method. It can be used to reconstruct an image from an irregularily sampled data set. It may therefore offer more accurate resampling than our averaging technique.

Initial test have been performed for non-circular based irregular geometries. We have obtained good results from these tests. But further work on other geometries, such as elliptical or rectangular, should also be done.

Bibliography

[1] S. Iijima, "Helical microtubules of grpahitic carbon," *Nature*, vol. 354, pp. 556–558, November 1991.

[2] A. G. Rinzler, H. J. Hafner, P. Nikolaev, S. G. K. L. Lou, D. Tomanek, T. D. Colbert, and R. E. Smallet, "Unraveling nanotubes: Field emission from an atomic wire," *Science*, vol. 269, no. 5230, pp. 1550–1553, September 1995.

[3] G. Z. Yue, Q. Qiu, B. Gao, Y. Cheng, J. Zhang, H. Shimoda, S. Chang, J. P. Lu, and O. Zhou, "Generation of continuous and pulsed diagnostic imaging x-ray radiation using a carbon-nanotube-based field-emission cathode," *Applied Physics Letters*, vol. 81, no. 2, pp. 355–357, July 2002.

[4] S. B. Sinnott and R. Andrews, "Carbon nanotubules: Synthesis, properties, and applications," *Critical Reviews in Solid State and Material Sciences*, vol. 26, no. 3, pp. 145–249, July 2001.

[5] D. Hongjie, "Carbon nanotubules: Synthesis, integration, and properties," *American Chemical Society*, vol. 35, no. 12, pp. 1035–1044, December 2002.

[6] J. M. N. Sinha and J. T. W. Yeow, "Carbon nanotubule based sensors," *Journal of Nanoscience and Nanotechnology*, vol. 6, no. 3, pp. 573–590, 2006.

[7] N. Sinha and J. T. W. Yeow, "Carbon nanotubes for biomedical applications," *IEEE Transactions on Nanobioscience*, vol. 4, no. 2, pp. 180–185, June 2005.

[8] M. Strck, "Types of Carbon Nanotubes." [Online]. Available:

[9] M. Kociak, A. Y. Kasumov, S. Gueron, B. Reulet, I. I. Kodos, Y. B. Gorbatov, V. T. Volkov, L.Vaccarini, and H. Bouchiat, "Superconductivity in ropes of single-walled carbon nanotubes," *Physical Review Letters*, vol. 86, no. 11, pp. 2416–2419, March 2001.

[10] C. Jianwei, T. Cagin, and W. Goddard III, "Thermal conductivity of carbon nanotubes," *Nanotechnology 11*, vol. 2, pp. 65–69, June 2000.

[11] R. S. Ruoff and D. C. Lorents, "Mechanical and thermal properties of carbon nanotubes," *Carbon*, vol. 33, no. 7, pp. 925–930, February 1995.

[12] C. Herring and M. H. Nichols, "Thermionic emission," *Review of Modern Physics*, vol. 21, no. 2, pp. 185–270, April 1949.

[13] E. L. Murphy and J. R. H. Good, "Thermionic emission, field emission, and the transition region," *Physical Review*, vol. 102, no. 6, pp. 1464–1473, January 1956.

[14] A. Rao, "CT-scanner." [Online]. Available: http://www.mscd.edu/ biology/3000course/webportfolio/webportfolio.html

[15] P. Toft, "The radon transform - theory and implementation," Ph.D. dissertation, Technical University of Denmark, 1996.

[16] J. Beutel, H. L. Kundel, and R. L. van Metter, Eds., *Handbook of Medical Imaging*. SPIE Press, 2000, vol. 1.

[17] J. Botfeldt and B. Kramer, Eds., *The elementary charge, in Units and Fundamental Constants in Physics and Chemistry*. Springer-Verlag, 1992, vol. : Subvolume b: Fundamental Constants in Physics and Chemistry.

[18] J. A. Bearden, "X-ray wavelengths," *Reviews of Modern Physics*, vol. 39, no. 1, pp. 78–84, January 1967.

[19] J. W. Motz, "Bremsstrahlung polarization measurements for 1.0-mev electrons," *Physical Review*, vol. 104, no. 3, pp. 557–562, November 1956.

[20] R. Y. Yin, O. Gabriel, and R.H.Pratt, "High-energy atomic photoelectric effect and bremmstrahlung," *Physical Review A*, vol. 36, no. 3, pp. 1207–1219, August 1987.

[21] G. S. Khandelwal, "Characteristic x-ray production in the atomic k shell," *Physical Review*, vol. 167, no. 1, pp. 136–138, March 1968.

[22] S. J. Blakeway, W. Gelletly, H. R. Faust, and K. Schreckenbach, "Studies of the photoelectric effect at high energy," *Journal of Physics B: Atomic and Molecular Physics*, vol. 16, pp. 3752–3765, May 1983.

[23] F. Reinert and S. Hufner, "Photoemission spectrosocopy-from early days to recent applications," *New Journal of Physics*, vol. 7, no. 97, pp. 1–34, April 1968.

[24] A. H. Warner, "Variation of the photoelectric effect with temperature and determination of the long wavelength limit for tungsten," *Physical Review*, vol. 33, no. 5, pp. 815–818, May 1929.

[25] D. L. Batchelar, W. Dabrowski, and I. A. Cunningham, *Medical Imaging 2000: Physics of Medical Imaging.* SPIE Press, 2000, ch. Tomographic imaging of bone composition using coherently scattered x rays, pp. 353–361.

[26] J. W. Motz and G. Missoni, "Compton scattering by k-shell electrons," *Physical Review*, vol. 124, no. 5, pp. 1458–1468, December 1961.

[27] C. L. Epstein, *Introduction to the Mathematics of Medical Imaging.* Pearson Education Inc., 2003.

[28] J. T. Kajiya and B. P. von Herzen, "Ray tracing volume densities," in *Proceedings of the 11th annual conference on Computer graphics and interactive techniques*, 1984, pp. 165–174.

[29] A. C. Kak and M. Slaney, *Principles of Computerized Tomogrpahic Imaging.* Society for Industrial and Applied Math, 2001.

[30] H. Schomberg and J. Timmer, "The gridding method for image reconstruction by fourier transformation," *IEEE Transactions on Medical Imaging*, vol. 14, no. 3, pp. 596–607, September 1995.

[31] The National Library of Medicine, "Visible human project: Male," September 2003.

[32] J. R. Fienup, "Invariant error metrics for image reconstruction," *Applied Optics*, vol. 36, no. 32, pp. 8352–8357, June 1997.